

A 64-CHANNEL PERSONAL COMPUTER BASED IMAGE RECONSTRUCTION
SYSTEM AND APPLICATIONS IN SINGLE ECHO ACQUISITION MAGNETIC
RESONANCE ELASTOGRAPHY AND ULTRA-FAST MAGNETIC RESONANCE
IMAGING

A Dissertation

by

NARESH YALLAPRAGADA

Submitted to the Office of Graduate Studies of
Texas A&M University
in partial fulfillment of the requirements for the degree of

DOCTOR OF PHILOSOPHY

May 2008

Major Subject: Electrical Engineering

A 64-CHANNEL PERSONAL COMPUTER BASED IMAGE RECONSTRUCTION
SYSTEM AND APPLICATIONS IN SINGLE ECHO ACQUISITION MAGNETIC
RESONANCE ELASTOGRAPHY AND ULTRA-FAST MAGNETIC RESONANCE
IMAGING

A Dissertation

by

NARESH YALLAPRAGADA

Submitted to the Office of Graduate Studies of
Texas A&M University
in partial fulfillment of the requirements for the degree of

DOCTOR OF PHILOSOPHY

Approved by:

Chair of Committee,
Committee Members,

Head of Department,

Steve Wright
Jim Ji
Mary McDougall
Takis Zourntos
Costas Georghiades

May 2008

Major Subject: Electrical Engineering

ABSTRACT

A 64-Channel Personal Computer Based Image Reconstruction System and Applications in Single Echo Acquisition Magnetic Resonance Elastography and Ultra-fast Magnetic Resonance Imaging. (May 2008)

Naresh Yallapragada, B.Tech (Honors), Indian Institute of Technology – Kharagpur;

M.S., University of Illinois at Chicago

Chair of Advisory Committee: Dr. Steven Wright

Emerging technologies in parallel magnetic resonance imaging (MRI) with massive receiver arrays have paved the way for ultra-fast imaging at increasingly high frame rates. With the increase in the number of receiver channels used to implement parallel imaging techniques, there is a corresponding increase in the amount of data that needs to be processed, slowing down the process of image reconstruction. To develop a complete reconstruction system which is easy to assemble in a single computer for a real-time rendition of images is a relevant challenge demanding dedicated resources for high speed digital data transfer and computation. We have enhanced a 64 channel parallel receiver system designed for single echo acquisition (SEA) MRI into a real-time imaging system by interfacing it with two commercially available digital signal processor (DSP) boards which are capable of transferring large amounts of digital data via a dedicated bus from two high performance digitizer boards. The resulting system has been used to demodulate raw image data in real-time data and store them at rates of 200 frames per second (fps) and subsequently display the processed data at rates of 26 fps. A further interest in real-time reconstruction techniques is to reduce the data handling issues. Novel ways to minimize the digitized data are presented using reduced sampling rate techniques. The proposed techniques reduce the amount of data generated by a factor of 5 without compromising the SNR and with no additional hardware. Finally, the usability of this tool is demonstrated by investigating fast imaging applications. Of particular interest among them are MR elastography applications. An exploratory study of SEA MRE was done to

study the temperature dependency of shear stiffness in an agarose gel and the results correlate well with existing literature. With the ability to make MRE images in a single echo, the SEA MRE technique has an advantage over the conventional MRE techniques.

DEDICATION

To my beloved Gurudev, His Holiness Sri Sri Ravi Shankar, and
To all teachers: past, present and the future

यतः सर्वाणि भूतानि प्रतिभान्ति स्थितानि च
यत्रै वो पाशमम् यान्ति तस्मै सत्यात्मने नमः

*Yatah sarvani bhutani pratibhanti stithani cha
yatray vo pasamam yanti tasmai satyatmane namah*

*Salutations to that reality in which all the elements, and all the animate and inanimate
beings shine as if they have an independent existence, and in which they exist for a time
and into which they merge.*

‘Vasistha’s Yoga’.
by Swami Venkatesananda,
State University of New York Press, Albany, NY

ACKNOWLEDGEMENTS

This is truly a special moment in my life. Thanking all those who have contributed to my growth as an engineer, a researcher, a student, a friend and most importantly as a human being, enough, is a task which I can barely accomplish. I am a very fortunate person to have received more than what I deserve. I have had the best teachers I could ask for, all my through my life, the best parents and the best of friends.

I acknowledge my advisor, Dr. Steve Wright. No matter how much I write about him, I cannot truly express the gratitude I feel for him. It is an honor to have him as my advisor. He is a rare combination of knowledge, patience, perseverance and humor. He has inspired me just by his presence. His immense trust and confidence in me made me set newer and higher goals for myself.

I thank my committee members, Dr. Mary McDougall, Dr. Jim Ji and Dr. Takis Zourntos, for all the support and the time off from their busy schedules. A special thanks to Dr. Arum Han for making it to my defense exam.

I have had very great experiences studying and living in College Station. I owe it all to my wonderful friends and lab members, who have enriched my life. I gratefully acknowledge all my friends at MRSL, John Bosshard in particular, friends from Art of Living in the US as well as in India.

I feel strange thanking my family. They are an inseparable part of me and I am a part of them. It is like thanking my heart for being my heart!

The one person to whom I truly owe everything to, whom I thank from every cell of my being is, my mentor, my Gurudev, His Holiness Sri Sri Ravi Shankar. Sri Sri is the most wonderful person in my life. His unconditional love, infinite wisdom, playful innocence and tireless service have transformed me in ways I could have never imagined. Sri Sri gave me the experience of my self, lighted the flame of never ending enthusiasm and joy. Whatever I was, am and ever will be, is because of my Gurudev.

TABLE OF CONTENTS

	Page
ABSTRACT.....	iii
DEDICATION.....	v
ACKNOWLEDGEMENTS.....	vi
TABLE OF CONTENTS	vii
LIST OF FIGURES.....	ix
LIST OF TABLES	xii
CHAPTER	
I INTRODUCTION.....	1
I.1 Rapid MR Imaging and Current Limitations.....	1
I.2 Dissertation Objective and Structure	3
II BACKGROUND	6
II.1 Conventional MR Imaging.....	6
II. 2 Parallel Imaging.....	10
II.3 Single Echo Acquisition MRI	13
II.3.1 Data Acquisition Hardware Setup.....	15
II.3.2 Data Acquisition and Image Reconstruction	18
II.3.3 Limitations of the Current SEA Processing Techniques	19
III RECONSTRUCTION SYSTEM FOR SEA IMAGING	22
III.1 Rapid Imaging Hardware Setup.....	23
III.2 Software Setup	25
III.2.1 Digital Demodulation Algorithm.....	25
III.2.1.1 Data Transfer Challenges.....	26
III.2.1.2 Mixing Down to Baseband.....	29
III.2.1.3 Low Pass Filtering	31
III.2.1.4 Convolution Challenges.....	32
III.2.1.5 Decimation	33
III.3 Other Challenges	36
III.4 Symphony Software Setup.....	39

CHAPTER	Page
IV	IMPROVEMENTS IN DATA HANDLING ISSUES BY REDUCED SAMPLING RATE METHOD44
	IV.1 Materials and Methods45
	IV.2 Results46
V	APPLICATIONS TO MAGNETIC RESONANCE ELASTOGRAPHY52
	V.1 Magnetic Resonance Elastography and Current Limitations.....52
	V.2 MRE of Agarose Gel During Thermal Ablation53
	V.2.1 Materials and Methods54
	V.2.2 Results59
	V.2.3 Discussion.....60
VI	FUTURE WORK AND CONCLUSIONS65
	REFERENCES.....67
	VITA.....75

LIST OF FIGURES

FIGURE	Page
2.1 A spin isochromat population aligned in the direction of z-oriented static field \mathbf{B}_0 gets tipped from minimum energy position towards the xy-plane.....	8
2.2 When the external excitation field is removed, the magnetization vector returns to its original equilibrium position governed by the time constants T_1 and T_2	9
2.3 A standard spin-echo pulse sequence depicting a series of RF pulses along with magnetic field gradients	9
2.4 Kspace information is obtained using a conventional spin-echo sequence	11
2.5 Parallel imaging techniques employ multiple coils and reduce imaging time by acquiring fewer number of phase encoding lines	12
2.6 Each planar pair element which makes up the 64 channel coil array is 2mm x 8.1cm long	13
2.7 The 64 channel single echo acquisition coil array consists of 64 planar pair coils each being 2mm x 8.1cm long	14
2.8 Echoes obtained from each of the 64 channels are stacked one above the other and are 1-D FFTed to obtain the SEA image	14
2.9 Schematic of a single channel receiver	15
2.10 The 200MHz signal obtained from the SEA coil is mixed down to an IF of 500KHz	16
2.11 A photograph of the 32 channel ICS-645 digitizer	17
2.12 Data flow architecture of the ICS-645	17
2.13 The value of the phase compensation determines the SNR of a SEA image	20
3.1 A picture of the TS-P36N DSP board	23
3.2 A picture of the host computer with one digitizer and DSP board connected via the FPDP connector	24

FIGURE	Page
3.3 A block diagram showing the data flow paths in the reconstruction system	24
3.4 Block diagram of the digital demodulation algorithm executed by the DSP board	25
3.5 Block diagram showing the format of data received via FPDP	27
3.6 Schematic of a single PC data handling system consisting of a multi-channel digitization board and a signal processing board	28
3.7 Echo data obtained from channel 47 from one of the experiments	30
3.8 Results of the echo after multiplying with sine and cosine functions	31
3.9 FIR filter characteristics showing the magnitude and the phase responses	32
3.10 Shown are the Inphase and the Qphase signals after removing the upper sideband by convolving with a low pass FIR filter	34
3.11 Shown are the Inphase and the Qphase signals after removing the upper sideband by convolving with a low pass FIR filter	35
3.12 The processed data from each channel is 1-D FFT-ed to yield of the profile of the imaging object	35
3.13 Digitized data from two of the 64 channels is shown, one from each of the ICS-645 boards	37
3.14 Shown are the images (from right to left) reconstructed from the console (a) and images reconstructed from data sampled at 2.5MHz (b), 1.875MHz (c) and 1.25MHz (d) respectively	38
3.15 The settings menu with the imaging variables	40
3.16 The ICS menu with various fields	41
3.17 The DSP menu	42
4.1 Digitized echo at 1.25MHz shown along with its profile after processing	47
4.2 Digitized echo at 1MHz shown along with its profile after processing	47

FIGURE	Page
4.3 Digitized echo at 0.75MHz shown along with its profile after processing	48
4.4 Digitized echo at 0.5MHz shown along with its profile after processing	48
4.5 Digitized echo at 0.25MHz shown along with its profile after processing	48
4.6 Shown are SEA images reconstructed by varying IF and sampling rates for 5 different configurations	49
4.7 Frequency response of one of the 64 channel receivers for a -10dbm input, 0Mhz span for center frequencies of 500, 400, 300, 200, 100, 90, 80, 70, 60, 50, 40, 30, 20, 10, 5, 0 KHz	50
5.1 The shear waves were generated using a sinusoidal voltage supplied to a solenoid oriented along the x-axis, orthogonal to the B0 field	55
5.2 The picture shows the transmit volume coil with the top removed, the 64 channel SEA receiver coil, and the agarose gel phantom with the vibrating plexiglass wedge	56
5.3 The 200Hz frequency vibrations start 10ms before the pulse sequence	57
5.4 A phase contrast image obtained from subtracting two SEA images with positive and negative motion encoding gradients	58
5.5 Shown are four phase contrast images at time instances of 10, 20, 30 and 40 minutes from the beginning of the heating	59
5.6 The Elastograms are obtained for a selected region of interest (ROI)	61
5.7 The temperature was obtained using the PRF method	62
5.8 The drop in shear modulus with time is greater in portions of the gel closer to the heat source (row 3) when compared to the ones further away (row 26)	62
5.9 Comparison of shear modulus of the ROI in frame 1 and frame 950	63

LIST OF TABLES

TABLE	Page
3.1 A comparison of the SNR values obtained from images sampled at three different sampling rates and the console reconstruction	38
4.1 SNR comparison of the images obtained at 5 different sampling rates	49

\

CHAPTER I

INTRODUCTION

Magnetic resonance imaging (MRI) techniques have quickly evolved into a key diagnostic modality due to their non-invasive and non-ionizing nature and also due to great improvements in imaging time in recent years. Emerging technologies in parallel MRI with massive receiver coil arrays have paved the way for ultra-fast imaging at increasingly high frame rates. But with the increase in the number of radio-frequency (RF) coil arrays and receiver channels to implement fast imaging methods, there are various challenges. This includes selecting optimal imaging parameters, processing large amounts of data, matching and tuning of these large arrays, to name a few. With the ability to collect images at huge frames rates, MRI gives the advantage of studying fast changing phenomena at high temporal resolutions. The ultra-fast frame rates have made imaging non-periodic and short-life events a possibility. This dissertation aims at addressing with a type of ultra-fast MRI and in the process, investigate the kind of applications that can be studied.

I.1 Rapid MR Imaging and Current Limitations

The primary factor which propelled MRI in becoming a major imaging modality today is the improvement in imaging time. From almost five hours to produce the first image in 1977 to a matter of a few seconds in the present days, the speed at which the images are obtained has greatly influenced its progress as a research and a clinical tool. The research into shortening the imaging time started by working on quicker and efficient ways to traverse the k-space, techniques such as the echo-planar imaging (EPI) and fast low-angle shot (FLASH) techniques were developed. Using the EPI technique, one of the most quickest ways to traverse the k-space, researchers were able to demonstrate one of the first real-time MR movies as early as 1982 (1). EPI demonstrated real-time imaging of coronary vessels with a temporal resolution of 35ms (2).

This dissertation follows the style of Magnetic Resonance in Medicine.

Whole-body and dynamic MR imaging studies using EPI were also demonstrated (3-8). But EPI did not become a widely used technique because of its demanding technical requirements on the gradients and susceptibility artifacts in the images. The gradient echo based FLASH technique which employs low power RF excitations, and hence smaller tip angles and lower data acquisition times, shortened the imaging time by almost two orders of magnitude. This enabled researchers to reconstruct images at 2 second intervals (9). The procedure was extended to rapid 3D imaging and imaging dynamic processes such as cardiac motion (10,11). MR fluoroscopy, an improvement of the FLASH technique was proposed by Riederer et.al (12,13). Other variations of the FLASH technique were also reported, such as by adding a sliding temporal window, a fully encoded gradient echo was acquired well within a second and real-time interactive MR, rapid blood flow imaging features were demonstrated (14-16). However, fast gradient switching techniques were seriously limited by safety standards. The safety limits for specific absorption ratio (SAR), which is a measure of RF energy deposition in human tissues, dictate the upper limit on the gradient duty cycle (17). So far all imaging was being done with a single receiver coil. In order to quicken the process of data acquisition, the use of multiple detectors to collect the MR signal was proposed as early as 1988. Multiple receiver coils circumvent the sequential acquisition of data by conventional MR. Work by Hutchinson et.al., Roemer et.al. and Wright et. al., (18-20) paved the way for a next generation of MR technology called parallel imaging.

Parallel MRI technology can very well be called the second generation MRI. Multiple sensors accelerated imaging time and opened up avenues for exciting imaging applications. Reduced scan time in parallel MRI was achieved by reducing the number of phase-encoding lines acquired during imaging. Fewer number of phase encoding lines from a coil result in an aliased image, but using the data obtained from multiple coils a deterministic image can be reconstructed. Theoretical work regarding the feasibility of this idea was demonstrated by Hutchinson and Raff with a large number of closely spaced detector loops (18). The foundation research work for the phased array concept discussing the advantages in terms of large field-of-view and SNR gain was laid by Roemer et al., and Wright et al(19,20). Work by Carlon and Minemura in 1993

demonstrated by reconstructing an un-aliased image with reduced number phase encoding lines using a two channel coil(19). In the subsequent years to come, new imaging techniques involving multiple coils and signal processing algorithms to combine the array data were proposed by many research groups (19-32). These algorithms mainly fell into two categories depending on the where the alias correction took place. Algorithms such as GRAPPA, SMASH, AUTO-SMASH, VD-AUTO-SMASH (22,26,31,32) were proposed to combine the aliased data in the k-space domain, while SENSE and PILS unwrapped the data in the image domain (26,29).

Using parallel MRI technology many interactive, real-time applications such as real-time cardiac imaging, catheter tracking and rapid flow imaging were demonstrated (33-48). As the number of channels employed for parallel MRI grew to 32,64 and even 96 (30,31,40,51,52), there was need to process the large amounts of data quickly while maintaining high signal fidelity. Digital receiver technologies which were introduced earlier were not economically feasible on commercial MRI systems as well as on research scanners with an increasing number of coil arrays (28,29,38,49-55). Some of the standard designs cost up to \$10,000 per channel (36,63-66). To avoid ‘ghosting’ of the data which was one of the major disadvantages of the analog quadrature mixers, the digital receiver technologies that were introduced consisted of very high speed Analog to Digital Converters (ADCs) along with digital FIR filters and high performance Digital Down Converters (DDCs) (34,49,50,56-60). The 64 channel receiver system built by Brown et al (29,61) is inexpensive compared to the models proposed before and can be easily assembled by many research groups. Together with the 64 channel coil built by McDougall and Wright, the system enables high temporal real-time imaging by completely eliminating phase encoding gradient in certain cases.

I.2 Dissertation Objective and Structure

The primary objective of this research work is to achieve ultra fast real-time imaging using the 64 channel receiver system and explore the applications that can be studied for diagnostic purpose. Four aims have been outlined for this dissertation:

Aim 1: Build a real-time image reconstruction system in a single computer.

Aim 2: Demonstrate real-time processing and image rendering at ultra-fast rates

Aim 3: Explore methods to reduce data handling issues by reduced sampling rate

Aim 4: Demonstrate the usability of the tool using Magnetic Resonance Elastography (MRE)

The dissertation consists of six chapters which describe the challenges faced in achieving the aims and discuss the results.

Chapter I : The chapter has introduced the importance of MRI in a clinical setting, and the rapid imaging technologies that were developed. A brief overview of parallel MRI has also been given along with the current restrictions on achieving real-time ultra-fast imaging using multiple receivers. The building of a real-time MR reconstruction system follows in the subsequent chapters.

Chapter II discusses the basic fundamentals of MRI needed for the reader to understand the research material, appreciate the challenges and the solutions presented. The chapter discusses k-space and image space, parallel imaging reconstruction techniques including SEA and its limitations. The chapter ends with a starting point for the following chapters.

Chapter III presents the building of a real-time reconstruction system. It describes the hardware setup and the software configurations. This is followed by the description of the data transfer techniques, the digital demodulation algorithm and the various stages in its development. Described in depth are the challenges faced at each stage and how they were overcome. The chapter also describes the user friendly ‘Symphony’ software setup and its various functions.

Chapter IV describes a clever method to reduce large amounts of data from being generated in multiple receiver systems. The method of imaging at reduced sampling rate is introduced which could be easily implemented in many commercial and research scanners without the need of expensive hardware infrastructure.

Chapter V presents one of the most significant achievements of this research work, the application of SEA to magnetic resonance elastography (MRE). The chapter introduces MRE, its importance, the work that has been done in this area by other groups and its current limitations. The chapter then presents the advantages of doing MRE using the SEA technique, the experiments done, particularly tissue stiffness dependency on temperature and the results obtained.

Chapter VI summarizes the research work and discusses the future prospects of SEA imaging, receiver technologies and applications.

CHAPTER II

BACKGROUND

In this chapter, the relevant background for the research work will be presented. The chapter will begin with the basics of NMR theory, the Bloch equations and NMR signal equation. The necessary information about k-space and image reconstruction will then be discussed. Of particular interest here is the equation involving the scan time in an imaging experiment. Parallel MRI will be introduced as a means to reduce the scan time by acquiring fewer k-space lines, leading to the SEA imaging technique. Then, the SEA method of data acquisition and reconstruction will be explained. Finally the constraints posed by the existing SEA reconstruction setup will be discussed. These topics are meant to be brief primer for the reader about MRI and parallel imaging, just enough to understand the research work to be presented in the chapters to come. An elaborate discussion of these principles is available in the literature.

II.1 Conventional MR Imaging

The information necessary to obtain an MR image is obtained by placing the object of interest in a static magnet field of strength \mathbf{B}_0 (a vector) and applying a series of RF pulses \mathbf{B}_1 together with magnetic field gradients. In the presence of a magnetic field, the protons spin with a frequency determined by the Larmor equation :

$$\omega = \gamma \mathbf{B}_0 \quad [2.1]$$

where ω is the angular frequency vector and γ is the gyromagnetic ratio of the proton. For ^1H proton, which is also the most used widely proton for imaging purposes, this value is $2\pi \times 42.5759 \text{ MHz/Tesla}$. This translates to a Larmor frequency of 200.238 MHz for the 4.7T magnet situated in the Magnetic Resonance Systems Lab (MRSL).

In the presence of the static B_0 , the proton population aligns itself according to the Boltzmann distribution, resulting in a slightly more than half of the isochromat population aligning in the direction of the external field. This is also the minimum energy

state and the rest of the population aligning in the opposite direction of \mathbf{B}_0 . When an external rotating RF field \mathbf{B}_1 (vector) is applied at the resonant frequency orthogonal to the direction of \mathbf{B}_0 , the minimum energy protons tip away from equilibrium. The tip angle depends on the strength and time duration of the applied external RF field. Figure 2.1 demonstrates this phenomenon of the spinning isochromats tipping because of the external field. The figure shows the combined magnetization vector \mathbf{M}_0 (B_0 is assumed to be z-directed which forces \mathbf{M}_0 also to be in the same direction) which is the sum total of individual spin magnetic moments μ_i (vectors), tipping towards the xy-plane on the application of \mathbf{B}_1 .

When the external RF field is removed, the spins which are now tipped away from the z-direction return to their equilibrium position. This relaxation procedure is governed by two time constants T_1 and T_2 . The time constant T_1 refers to the growth of the z-directed longitudinal component of the magnetization vector (\mathbf{M}_z) and is also known as the spin-lattice relaxation time. The time constant T_2 refers to the decay of the vector in the transverse xy component (\mathbf{M}_{xy}) and is known as the spin-spin relaxation time. Mathematically, they are represented as the Bloch equations:

$$\mathbf{M}_z = \mathbf{M}_0 \cos(\alpha) (1 - e^{-t/T_1}) \quad [2.2]$$

$$\mathbf{M}_{xy} = \mathbf{M}_0 \sin(\alpha) e^{-t/T_2} \quad [2.3]$$

For an observer in the stationary frame, the magnetization vector itself is spinning at the Larmor frequency while returning back to its original equilibrium position. The trajectory traced by the tip of the magnetization vector is shown in Figure 2.2.

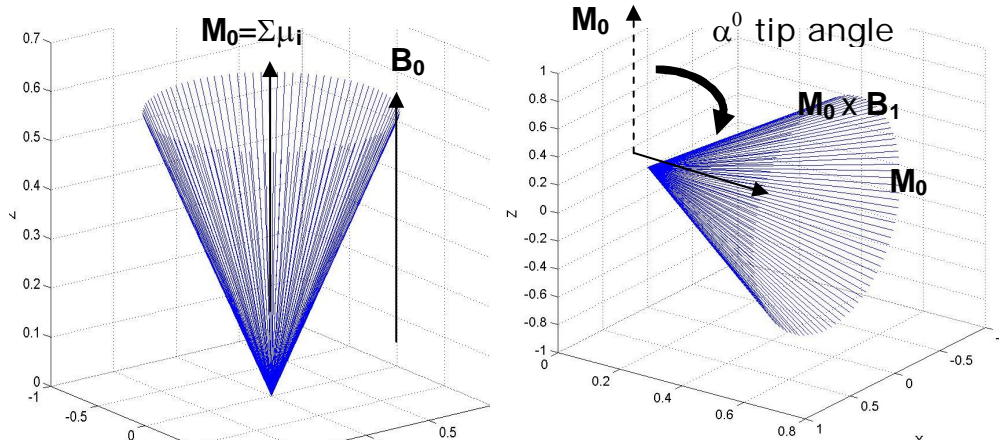


Fig 2.1 A spin isochromat population aligned in the direction of z-oriented static field B_0 gets tipped from minimum energy position towards the xy-plane. The extent of the α^0 tip angle depends on the strength and the duration time of the external rotating magnetic field B_1 .

If a probe is placed near the phantom, the relaxing magnetization of the protons induces a voltage, this is the NMR signal. Image formation from this NMR signal is done by spatially localizing the signal with the use of magnetic field gradients (G_x , G_y and G_z), a work pioneered by Dr. Lauterbur (62). A standard spin-echo pulse sequence to generate an $N_p \times N_f$ image, where N_p is the number of phase encoding and N_f is the number of frequency encoding steps, involving a set of RF pulses and field gradients is shown in Figure 2.3. It illustrates the application of a 90 degree RF pulse together with a slice selecting gradient (G_s), which are followed by phase (G_p) and frequency (G_f) encoding gradients. To get an echo from the phantom, the dephased spins are subjected to a 180 degree refocusing RF pulse and the signal recorded during the read-out gradient, with the echo peak occurring at time TE.

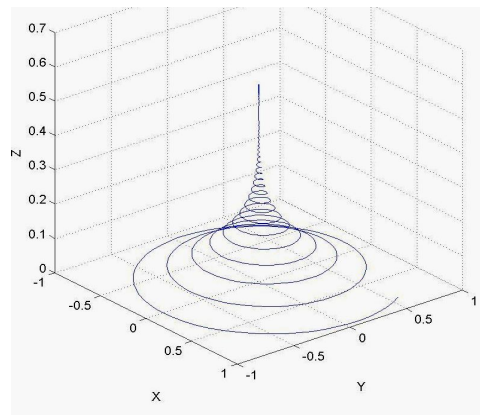


Fig 2.2 When the external excitation field is removed, the magnetization vector returns to its original equilibrium position governed by the time constants T_1 and T_2 . Shown is the trajectory of the magnetization vector as it relaxes from a 90° tip.

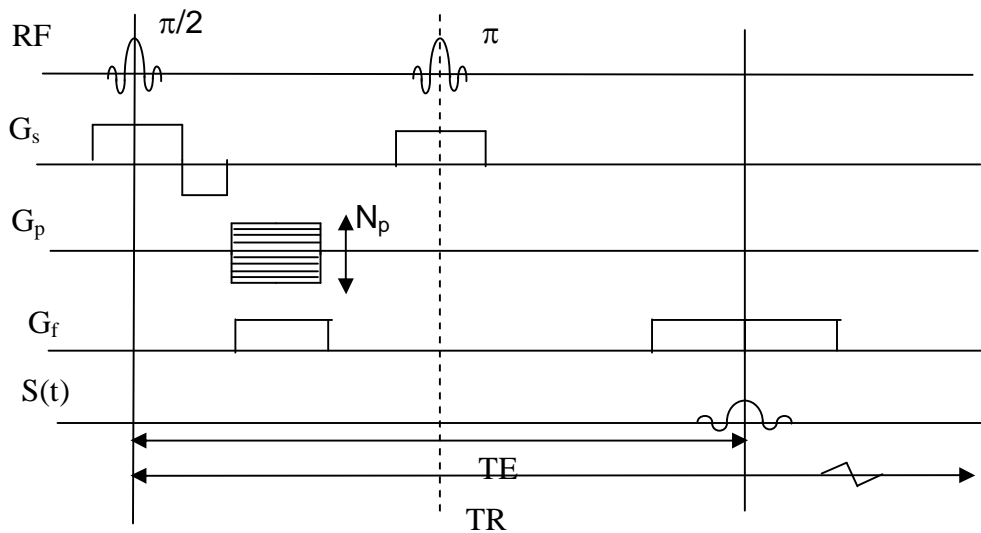


Fig 2.3 A standard spin-echo pulse sequence depicting a series of RF pulses along with magnetic field gradients. The sequence is repeated for N_p number of times for varying values of phase encoding gradient G_p at TR intervals. The resultant echo is sampled for N_f number of points.

The signal which is being recorded by the receiver RF coil has all the frequency and phase information that is necessary to spatially localize it. The received signal $S(t)$ can be mathematically expressed as:

$$S(t) = \iint_{\text{Slice}} I(x, y) e^{-j((\omega_0 - \omega_{\text{ref}})t + \gamma G_x x t + \gamma G_y y T_p)} dx dy \quad [2.4]$$

where $I(x, y)$ is the image of the object, G_x and G_y are the frequency and phase encoding gradients respectively, T_p is the time duration of the phase encoding gradient, ω_0 and ω_{ref} are respectively the Larmor and receiver mixing frequencies. The equation can be simplified to a 2D fourier transform relationship by making the mixing or demodulating frequency to ω_0 . Hence the signal simplifies to the standard ‘k-space’ notation (the frequency and the phase encode times have been made equal for a more simplified version of the equation):

$$S(k_x, k_y) = \iint_{\text{Slice}} I(x, y) e^{-jk_x x} e^{-jk_y y} dx dy \quad [2.5]$$

where $k_x = \gamma G_x t$ and $k_y = \gamma G_y T_p$. The signal obtained for each value of phase encoding gradient is sampled N_f number of times and this forms one line of the k-space. The entire k-space is filled by varying the value of G_y at TR time intervals. Hence the scan time is N_p times TR.

$$\text{Scan Time} = N_p \times \text{TR} \quad [2.6]$$

After obtaining the entire information, the data matrix is 2D Fourier transformed to obtain the image. An example demonstrating this is shown in Figure 2.4

II. 2 Parallel Imaging

The scan time in a typical MR experiment is in the order of a few minutes. As determined by equation 2.6, there are two ways to reduce this scan time: a) reduce TR and b) reduce N_p . Many research groups presented ways to shorten the TR time and also efficiently traverse the k-space. (1-8,10,16,18).

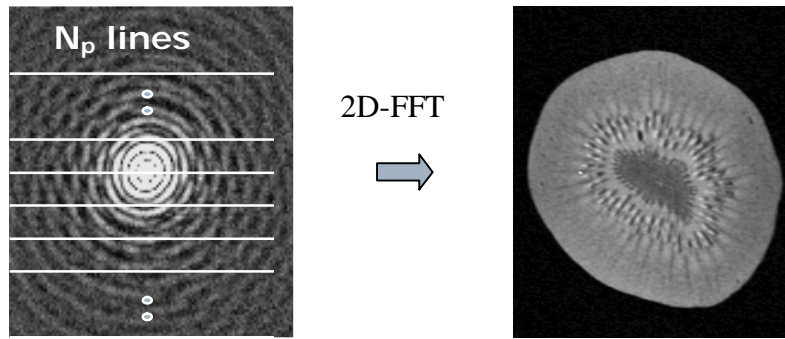


Figure 2.4 Kspace information is obtained using a conventional spin-echo sequence. After obtaining the information for each phase encoding value, the data is 2D fourier transformed to obtain the image.

Reducing TR not only compromises the image quality but raises a larger concern regarding human safety. The fast switching gradients and the quick succession of RF pulses result in high SAR (specific absorption ratio) (17), which is a measure of the energy deposited in the human tissue. The other alternative to reducing TR is reducing the number of phase encoding lines, N_p . This is done by having multiple sensors to receive the data instead of just one.

Parallel imaging reduces the scan time by acquiring fewer number of phase encoding lines from multiple receivers. The number of lines reduced is termed the reduction or the acceleration factor. As a fewer number of lines are collected instead of the entire data set, 2D fourier transforming the k-space data results in an aliased image. Since there are multiple sensors collecting the data, each receiver coil produces an aliased image. The original unaliased image can be reconstructed either in the image domain or in the k-space domain by using apriori information which is available in the form of the known spatially varying coil sensitivity distribution. For example, consider two coils being used instead of a regular volume coil. The coil sensitivities are shown in Figure 2.5, with the sensitivity region of each coil extending only up to half of the full FOV (63). When an acceleration factor of 2 is used, two halves of the original image are obtained simultaneously by both the coils which can now be combined using the coil sensitivity information of each to obtain the original image. Several research groups have proposed different methods of combining the information from multiple receiver coils. They can be categorized into two groups:

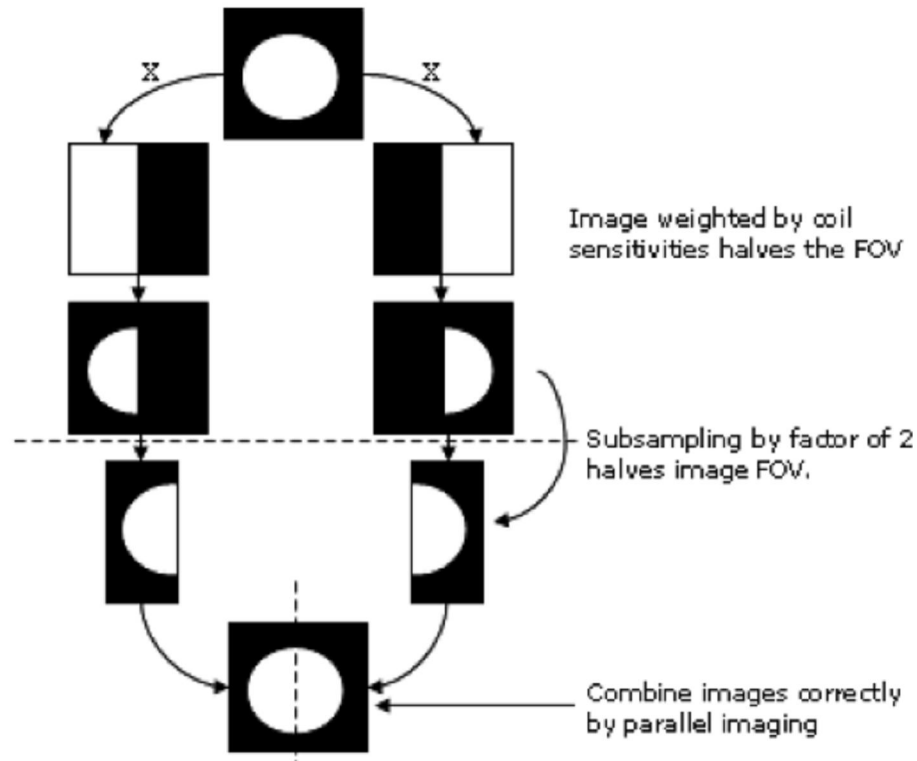


Figure 2.5 Parallel imaging techniques employ multiple coils and reduce imaging time by acquiring fewer number of phase encoding lines. The aliased data from each coil is combined according to their sensitivity distribution either in the image domain or in the k-space domain (63).

a) K-space domain correction

Missed lines in the k-space domain are reconstructed either for the original image or for images from each individual coil. Algorithms such as GRAPPA, SMASH, AUTO-SMASH, VD-AUTO-SMASH (24,28,33,34) are used to achieve this.

b) Image domain correction

In the image domain, coil sensitivity maps are used to ‘unfold’ each image. Algorithms such as SENSE, PILS and SEA use individual coil sensitivity information obtained apriori to combine the individual images (24,27).

II.3 Single Echo Acquisition MRI

The 64 channel parallel imaging technology developed in MRS_L marks the beginning of Single Echo Acquisition (SEA) MRI (29). The SEA coil array consists of 64 planar pair elements designed in such a way that the field profile of each element is highly localized, without any overlapping sensitivity regions with adjacent elements. Figure 2.6 shows an element of the array, the field and phase profiles across the coil. The frequency encoding or the read-out direction is along the length of the coil. However it can be seen from the figure that the coil has a non-zero phase across its width.

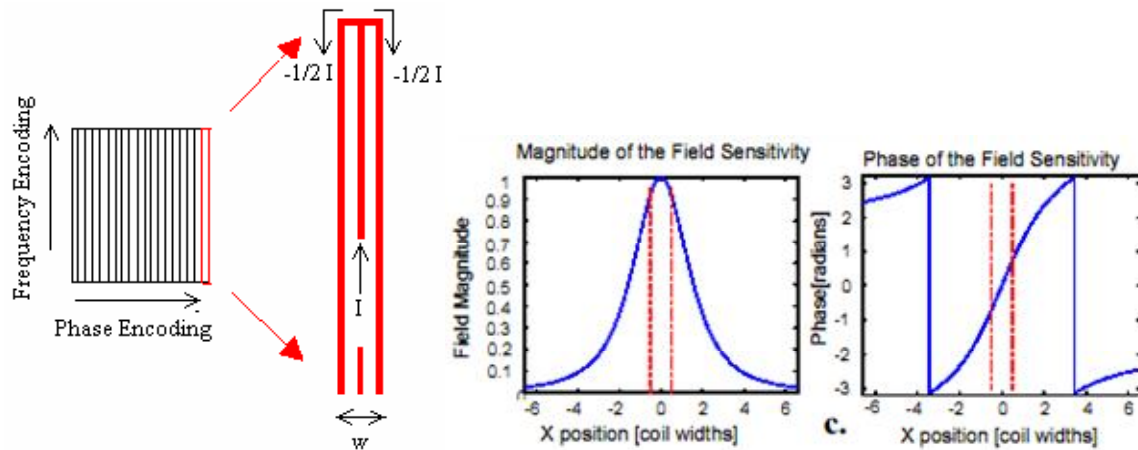


Figure 2.6 Each planar pair element which makes up the 64 channel coil array is 2mm x 8.1cm long. The field profile across the coil width is very narrow and does not overlap with the sensitivities of adjacent coils (awaiting permission from IEEE).

Figure 2.7 shows an example of the 64 channel coil. Each element is matched to 50Ω impedance and tuned to Larmor frequency. Since the coil sensitivities are highly localized, the signal picked up each coil is protons right above the coil and there is no information overlap between any two coils. Reconstructing an image from the 64 SEA coils is unlike any method mentioned above. In SEA imaging, every coil collects a different k-space line, which, when all put together, form the complete k-space data. With just one RF excitation the 64 SEA coils record 64 lines of k-space (Fig 2.8). Therefore, the image size will be a $64 \times N_f$, where N_f is number of samples in the read-out direction.

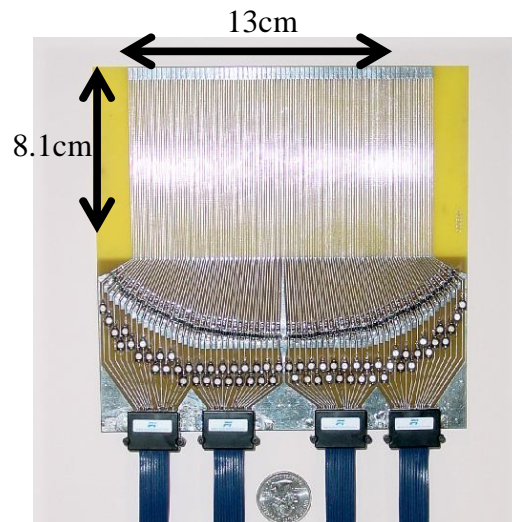


Figure 2.7 The 64 channel single echo acquisition coil array consists of 64 planar pair coils each being 2mm x 8.1cm long. The entire array ensemble is 8.1cm x 13 cm long (64).

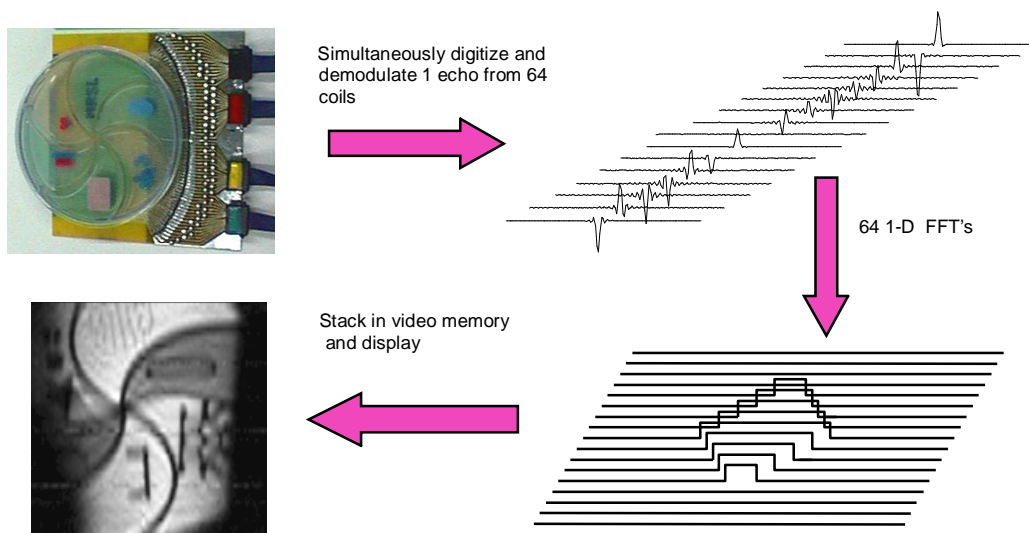


Figure 2.8 Echoes obtained from each of the 64 channels are stacked one above the other and are 1-D FFTed to obtain the SEA image. Very narrow field profiles enable this single shot imaging technique (64).

II.3.1 Data Acquisition Hardware Setup

The NMR signal induced in the receiver coil is centered at the Larmor frequency i.e. 200MHz and having a finite bandwidth determined by the imaging parameters. It is possible to detect this signal at 200MHz by direct digitization. This however, would require high speed, high performance ADCs digitizing at the Nyquist rate of 400MHz, which, would not only be cost prohibitive but also generate large amounts of data even for detecting a short echo. For example, to digitize an echo of 1.28 ms, having a bandwidth of 100KHz, at 400MHz sampling frequency, would generate 512000 samples and if this is done using a 16-bit digitizer, it would mean 1000KB per echo per channel. For the 64 channel SEA coil, this would be 62.5Mbytes per echo. The huge amount of data digitized would also translate to delays in terms of transferring the data via the throughput channels and increased computation time. In order to avoid large amounts of data being generated during digitization, the NMR signal must be down converted to a lower frequency.

A 64 channel mixer designed by Brown et al down converts the 200MHz NMR signal to 500 KHz Intermediate Frequency (IF) (61). Figure 2.9 shows the schematic of a single channel mixer consisting of a low noise amplifier, RF gain, downconverter, IF gain and filtering modules.

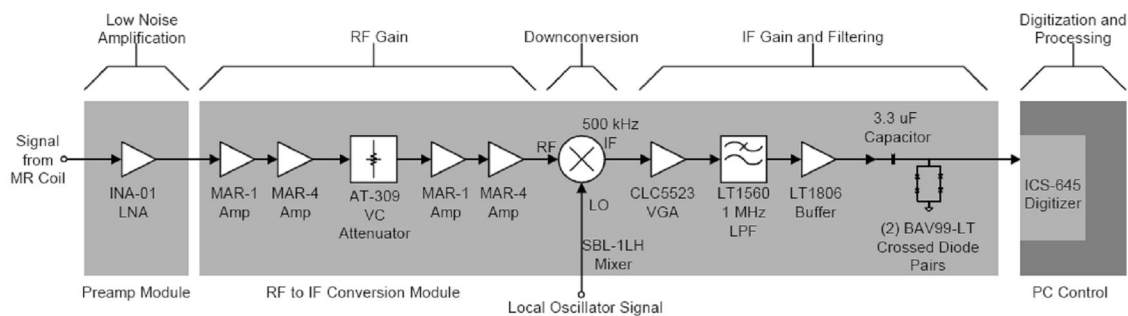


Figure 2.9 Schematic of a single channel receiver (65) .

The 200MHz NMR signal which has now been amplified and downconverted to 500KHz, can now be digitized without generating large quantities of data. Figure 2.10 shows two racks containing 32 mixers each and a computer equipped with with two 32 channel digitizers.



Figure 2.10: The 200MHz signal obtained from the SEA coil is mixed down to an IF of 500KHz. Components (a) and (b) contain 32 IF receiver channels. The data acquisition computer (c) is equipped with 64 channel digitizers.

The digitization of the 500KHz IF signal is done using a high performance digitizer card, the ICS-645 (GE Fanuc Embedded Intelligent Platforms Inc., Ottawa, Ontario, Canada) (66). The ICS-645 digitizer card is capable of sampling 32 channels at a maximum sampling frequency of 2.5MHz per channel when all the 32 channels are being sampled. The ICS-645 can also be configured for 16 channels with 5MHz/channel, 8 channels with 10MHz/channel or 4 channels with 20MHz/channel. A photograph of the digitizer is shown in Figure 2.11. The digitizer is a 32-bit 33MHz PCI 1.1 card, based on Analog Devices AD9260 chip (Analog Devices Inc., Norwood, MA) (67).



Figure 2.11 A photograph of the 32 channel ICS-645 digitizer. The digitizer is capable of a sampling at a maximum rate of 2.5MHz/channel (66).

As a parallel branch to the PCI data flow path, the card is also equipped with Front Panel Data Port (FPDP) capability. FPDP is a dedicated 32-bit data bus which allows the ICS-645 to communicate with other cards equipped with FPDP enabling data throughput rates of 160Mbytes/sec, far greater than 80-100Mbytes/sec possible via a shared PCI bus. Figure 2.12 shows the data flow path of the ICS-645.

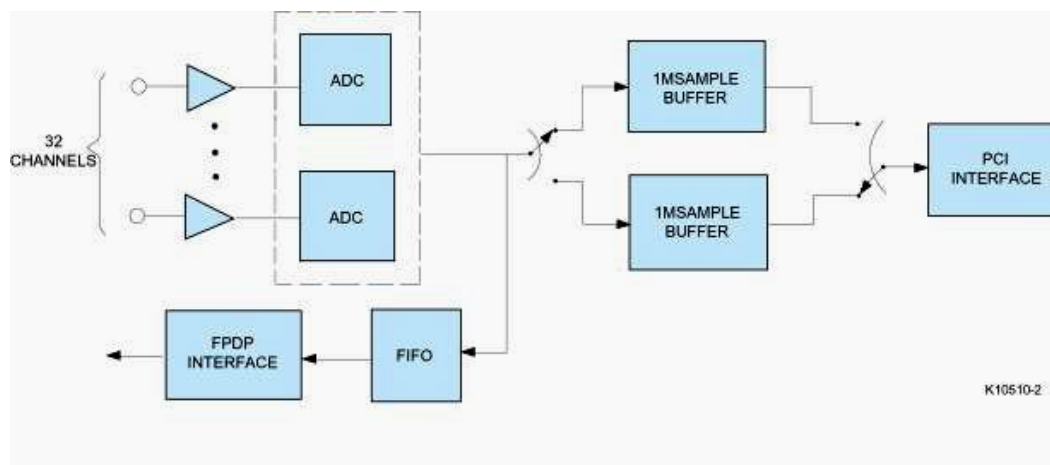


Figure 2.12 Data flow architecture of the ICS-645 (66).

The clock and trigger supply for the card can either be internal or external. In the case of an external clock, the supply frequency has to be twice the sampling rate (in the 1x oversampling mode). For example, if a 2.5 MHz/channel sampling frequency is desired, an external clock supply of 40MHz is needed, which is twice the 1x sampling rate of

20MHz. The sample size generated by the ICS-645 is 2 bytes and with each on-board memory bank having a capacity of 2Mbytes, a total of 2^{20} samples can be stored which translates to 32768 samples per channel when all the 32 channels are being digitized.

II.3.2 Data Acquisition and Image Reconstruction

The 200MHz MR signal which has been mixed down to a signal with 500 KHz center frequency is sent to the ICS-645 for digitization at a frequency of 2.5 MHz per channel. The time length of the MR signal is derived using the formula

$$\text{Echo length} = \text{Number of frequency encodes} / \text{desired spectral sidth} \quad [2.7]$$

For example a 256 frequency encodes, 50KHz bandwidth signal measures upto 5.12 millisecond in length. At a sampling rate of 2.5 MHz per channel this results in $5.12e-3 \times 2.5e+6 = 12800$ points per channel. The total data generated in digitizing 64 channels for 256 phase encodes or repetitions is

$$\underbrace{(2.56-3)}_{\text{Acquisition window}} \times \underbrace{(2.5e+6)}_{\text{Sampling frequency}} \times \underbrace{2}_{\text{bytes}} \times \underbrace{64}_{\text{Number of data points}} \times 256 = 400\text{MB!}$$

As the echoes are being digitized the data is copied from the onboard memory banks of the ICS-645 and written to the hard disk of the host computer. The software drivers for the operation of the ICS-645 and an example code were provided by the manufacturer. Using a modified version of the code, the digitized data is transferred from the onboard memory banks to the host computer's hard drive at the end of each echo acquisition.

The digitized data is not image domain data yet. The signals centered at 500KHz are processed to move them to baseband to obtain the demodulated k-space information. The baseband signal data belonging to each channel is then 1-D fourier transformed along the frequency encoding direction to obtain the profile of the object. The profiles from all the channels are combined to obtain the full image.

II.3.3 Limitations of the Current SEA Processing Techniques

Although the SEA technique provides an image in a snapshot, there are throughput bottlenecks when it comes to processing the data. These are particularly apparent during ultra-fast imaging. For example to make a high temporal resolution movie of a flow phantom, acquiring a 100KHz spectral width, 128 frequency encoded signal at a repetition time of 8millisecods (125 frames per second) for a duration of 1 minute, generates

$$\underbrace{(1.28-3)}_{\text{Acquisition window}} \times \underbrace{(2.5e+6)}_{\text{Sampling frequency}} \times \underbrace{2 \times 64}_{\text{bytes}} \times \underbrace{125 \times 60}_{\text{Number of repetitions}} \quad \boxed{\approx 3\text{GB!}}$$

Such a large amount of data poses a significant challenge in terms of processing, particularly if processing on a different computer. The problem gets further worsened when the imaging parameters need optimization. One of the important parameters which needs to be optimized in every SEA experiment is the value of the phase compensation gradient. This is needed because of a non-zero phase across the planar pair coils used for SEA. Figure 2.6 shows the phase profile across a coil. The phase across of the coil is cancelled using a particular value of the phase encoding gradient, as shown in (68). No or non-optimal compensation of phase results in a reduced SNR. The dependency of the SNR of the SEA image on the value of the phase compensation gradient was established by McDougall and Wright (68). Figure 2.13 shows the SEA image for three different values of phase compensation, the top image obtained for no gradient phase compensation, middle image for the optimal value and the bottom image for an overcompensated phase gradient.

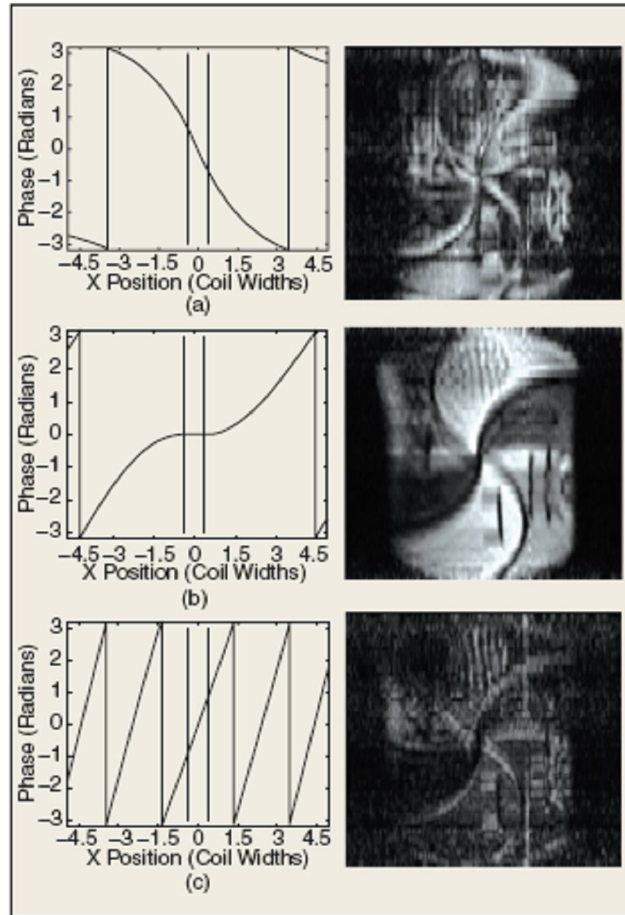


Figure 2.13 The value of the phase compensation determines the SNR of a SEA image. The phase across each coil element has to be zero for the best SNR. Shown are three images obtained from zero (top), optimal (middle) and overcompensated (bottom) phase gradients (awaiting permission from IEEE).

Finding the optimal value of phase compensation gradient is done at the beginning of every SEA experiment. The value is often decided by visually inspecting the image quality, for which raw data has to be first obtained and processed. With large amounts of data generated and with an un-automated data processing and image reconstruction procedures, selecting an optimal k-line value can be time consuming, greatly undermining the advantage of SEA imaging.

The huge amounts of data generated during a SEA imaging experiment is discouraging in experiments involving rapid imaging, MR microscopy, MR elastography. These are few of the topics this thesis is going to explore.

The next few chapters discuss various applications that can be studied with SEA imaging while keeping the generated data to a minimum. The following chapter reports building of a real-time data processing system. Quick data processing and image rendition is highly desirable in most of the experiments involving SEA and the chapter presents an easy, elegant and scalable solution using Digital Signal Processing (DSP) equipped boards.

CHAPTER III

RECONSTRUCTION SYSTEM FOR SEA IMAGING

In the preceding chapter various parallel imaging techniques were introduced and the SEA imaging technique was briefly discussed. One of the limitations of the SEA methodology is large amounts of data being generated in a short period of time. This is particularly a significant problem in high temporal resolution applications such as flow imaging, motion experiments, etc. If carefully examined, the bottleneck of the problem is the data throughput paths of the system. The Peripheral Component Interconnect (PCI) bus which is currently being used to move the digitized data for processing is unable to handle the rate of data generation. The PCI bus is a shared resource and with interrupt calls from various components and functions of the host computer, a practical bandwidth of 80Mbytes per second is insufficient to sustain the throughput for rapid SEA applications which can be upto 50 Mbytes per second. The solution to this problem is to reduce the amount of data transferred via the PCI bus. Data size reduction can be achieved by digitally demodulating the IF data to baseband. While the ICS-645 boards do not allow for any processing on-board, it is possible to transfer the data to a DSP board via routes other than the PCI bus. An alternative route to the PCI bus is available with the ICS-645 digitizers. A dedicated bus called the FPDP (Front Panel Data Port) is a platform independent 32-bit synchronous data flow path that allows throughputs of 160Mbytes per second. FPDP technology, engineered by Interactive Circuits and Systems (ICS) limited (Gloucester, Ontario, Canada), which is now GE Fanuc Embedded, is a cost-effective approach to data transfer problems, over moderate distances between boards. This chapter discusses the implementation of DSP as a solution to reducing the large amounts of digitized data. The chapter begins with a description of the hardware setup, the DSP board architecture, memory and data throughput limitations, digital demodulation algorithm, and the software construct. Along with these topics, the challenges faced in their implementation and the proposed solutions are discussed.

III.1 Rapid Imaging Hardware Setup

The signal processing board for real-time processing had to be FPDP compatible. For this reason, two TS-P36N boards were chosen (Transtech DSP Ltd, Ithaca, NY now Vmetro, Inc., Houston, TX) (69). A picture of the DSP board is shown in Figure 3.1. The TS-P36N is a 66 MHz, 64-bit PCI card equipped with four 300MHz Analog Devices DSP processors, the TigerSharc ADSP-TS-101s (Analog Devices Inc., Norwood, MA). The card has an on-board 256MB SDRAM while the individual TigerSharc processors have 6Mbits of SRAM of internal on-chip memory. The internal memory has been divided into 3 banks of 250Kbytes of memory space by the Transtech's compiler.

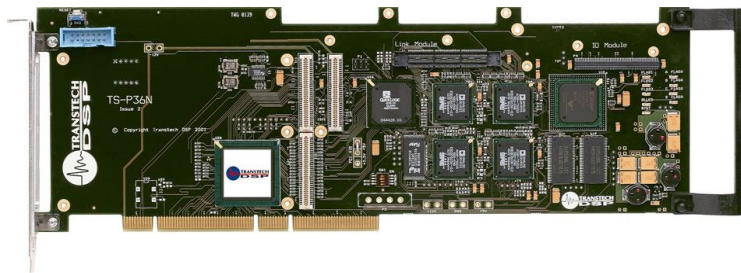


Figure 3.1 A picture of the TS-P36N DSP board. A quad cluster of TigerSharc ADSP-TS-101 processors, the board is equipped with a dedicated data bus for high speed data transfers of up to 160MB/sec.

Two TS-P36N boards were assembled along with two ICS-645 boards in a single computer. All the four boards are currently housed in a custom-built computer assembled with a SuperMicro X6DVL-G motherboard (Super Micro Computer Inc., San Jose, CA), two Intel Xeon-DP 2.8GHz processors (Intel Inc., Santa Clara, CA), two 1GB 333MHz DDR memory modules (OCZ Technology, Sunnyvale, CA) and Microsoft Windows XP professional operating system (Microsoft Corp., Redmond, WA). Figure 3.2 shows the system with one ICS-645 and TS-P36N boards with the FPDP ports connected via a cable.

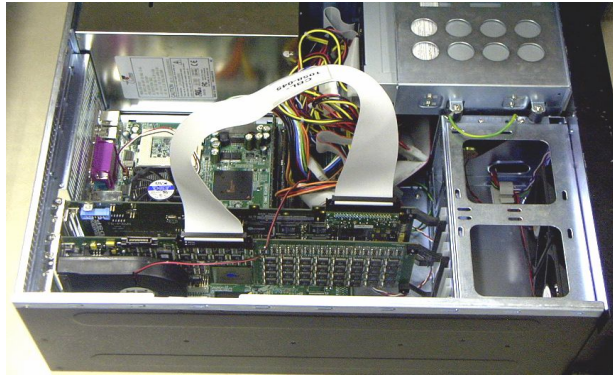


Fig 3.2 A picture of the host computer with one digitizer and DSP board connected via the FPDP connector.

A block diagram of the data flow paths in the system is shown Figure 3.3

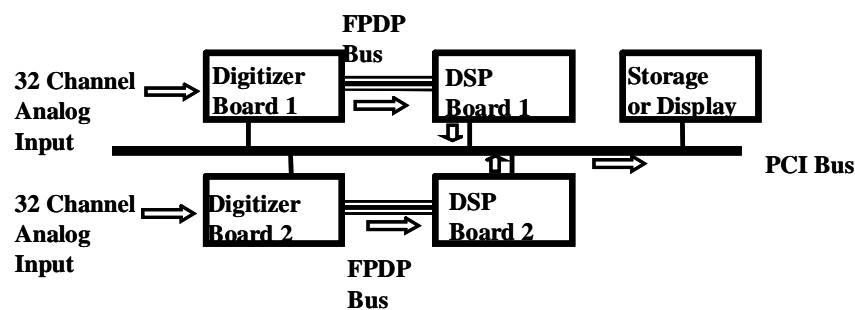


Fig 3.3 A block diagram showing the data flow paths in the reconstruction system.

Apart from the analog inputs, the digitizer require two more inputs, the trigger and the clock. The clock is supplied from a function generator SRS DS 345 (Stanford Research Systems, Sunnyvale, CA) which is phase locked to a 10MHz clock on the scanner console, while the trigger input is obtained from the magnet instrument console. The software drivers for the operation of the DSP boards were provided by Transtech, along with a C language compiler, linker modules and libraries.

The first step in using the DSP boards was to perform a hardware check and then load the FPGA firmware onto the boards to facilitate the FPDP transfer. Also, paths for various command directories and libraries had to be declared. All software code needed to program the processors were first written in C, then compiled and linked to generate a DSP executable filename.dxe file. This is done via a 'server' which runs on the host

machine. Once the .dxe file has been loaded, all is set for executing the digital demodulation algorithm.

III.2 Software Setup

The method of data transfer and processing was based on the type of application that was performed. The following is the method for ultra high speed reconstructions aimed at speeds of 125 frames per second or greater.

III.2.1 Digital Demodulation Algorithm

A block diagram of the digital demodulation algorithm implemented on the DSP boards is shown in figure 3.4. The digital demodulation algorithm works in the following way. Each echo centered at an intermediate frequency of 500KHz was digitized at 2.5MHz for the echo length. The echo length depends on the number of frequency encodes and the spectral width as determined by equation 2.7.

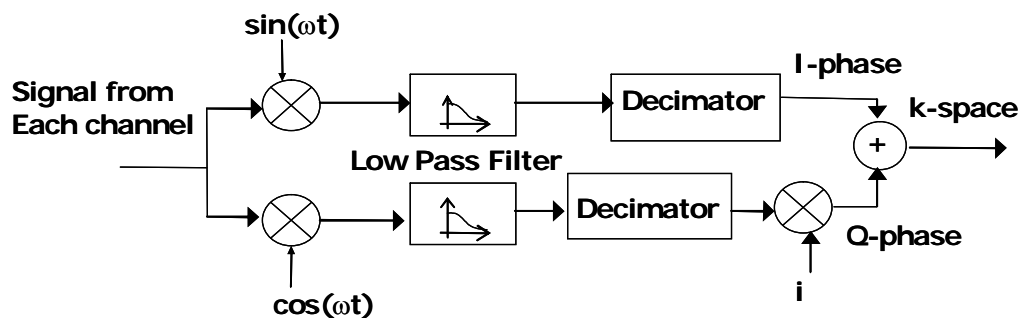


Fig 3.4 Block diagram of the digital demodulation algorithm executed by the DSP board. Signal from each channel is multiplied by sinusoidal functions low pass filtered and decimated, to obtain complex k-space data.

For example an echo with spectral width of 100KHz and 128 frequency encodes, translates to 3200 samples when digitized at 2.5MHz. This data was transferred to the DSP board via the FPDP bus rather than the PCI bus to save data transfer time, i.e. 3200 points per channel were acquired and transferred to the DSP. The data transmitted over the FPDP is made up of 4-byte words, that is, samples from two channels are sent as one entity. We have 32 channels being digitized hence we receive 16 words per sampling

instant. However, despite the speed there were a few disadvantages with the FPDP transfer to the DSP. These have been discussed below.

III.2.1.1 Data Transfer Challenges

The DSP compiler did not allow 2-byte short integers to be allocated. As a result, each digitized sample even though 2-byte long, had to be stored as a 4-byte integer. This is a serious drawback given the amount of actual data the DSP could have stored via the FPDP. With the FPDP data as 4-byte words (two 2-byte samples in one 4-byte entity) meant that the data corresponding to each channel had to be separated out because of the non-availability of 2-byte storage with the DSP (Fig 3.5). Since a 2 byte integer could not be allocated, the even and odd channels had to be separated for every sampling instant. This was done by the byte-separation method shown in equations 3.1 and 3.2. The process not only increased the memory usage by 100% but also resulted in an increase in the processing time.

$$\text{Even_Channels} = (((\text{Data_Pool} \gg 16) \& 0\text{xffff}) > 32767 ? (((\text{Data_Pool} \gg 16) \& 0\text{xffff}) - 65536) : ((\text{Data_Pool} \gg 16) \& 0\text{xffff}) \quad [3.1]$$

$$\text{Odd_Channels} = (((\text{Data_Pool}) \& 0\text{xffff}) > 32767 ? (((\text{Data_Pool}) \& 0\text{xffff}) - 65536) : ((\text{Data_Pool}) \& 0\text{xffff}) \quad [3.2]$$

Where Data_Pool is the data buffer obtained via FPDP transfer. Even_Channels and Odd_Channels are even and odd numbered channels respectively.

Another setback was because of firmware restrictions. The firmware which controls the Xilinx Virtex-2 FPGA interface for the FPDP was written in such a way that all the FPDP data was routed into the internal memory of processor A, which has three compartments of 250Kbytes each. The total FPDP transferred data size for 3200 samples (2 bytes per sample) across 32 channels would amount to $3200 \times 2 \times 32 = 200\text{Kbytes}$. With each bank having a space of 250Kbytes, only 4000 samples per channel could be stored which seriously limited the length of the acquisition window.

1. For more than a year since the DSP boards were being used, the FPDP transfer was not how it was supposed to be. The transfer generates more data in the DSP than generated by the digitizer. The occurrence of this extra information has been successfully figured out as a flaw in the ICS-645 digitizer board after a numerous consultations with ICS and Transtech engineers. Its been observed that for FrameCount =2, an extra 4 bytes of data occurs at the end of every 128 bytes. This observation has been consistent. Hence for 3200 samples generated by the digitizer there are 3300 samples received by the DSP. Therefore for 32 channels, the DSP receives 105600 number of samples. This error strained the availability of memory space on the already small processor space. The flaw was fixed by sending the ICS-645 digitizers to the manufacturer for repair. In the present hardware configuration the digitizers work as expected.

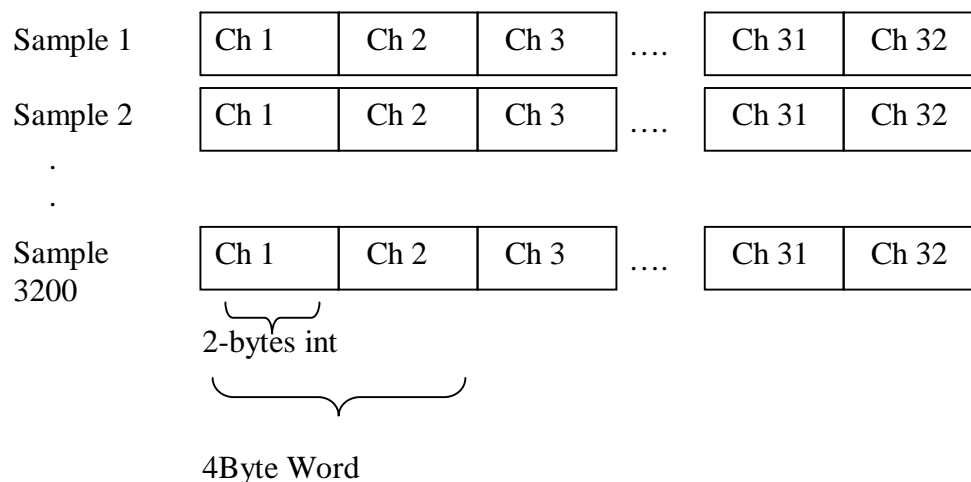


Fig 3.5 Block diagram showing the format of data received via FPDP. Two samples from consecutive channels are clubbed together as a 4byte word. 16 words are received per sampling instant.

2. For acquisition sizes larger than the 4000 samples per channel, the memory space available in the processor A is not sufficient. Various methods were tried to get around this problem.
 - a. Double buffering: The FPDP data pool was divided into two buffers. After filling one of the buffers, a thread program was executed which would divide the processor time in filling a second buffer while the data from the first buffer was processed. The

processing loop would continue with the second buffer while the first one gets filled. This solution proved ineffective as the processing time took much longer than the time for data transfer.

- b. Using other processors: Since it was concluded from the double buffering solution that processing power isn't able to catch up the data throughput rates, the idea of using the other processors B,C and D were tried out. The idea was to double buffer the FPDP data flowing into A into other processors. So while one of the buffers is being filled in A, the data from the other buffer would be moved to B, C and D for processing. This was achieved using link message handlers (Fig 3.6) and also semaphores. These are communication channels which allow data transfer and also messaging between processors signaling the start or finish of a process. This idea also fell short of time when compared to the FPDP data throughput.

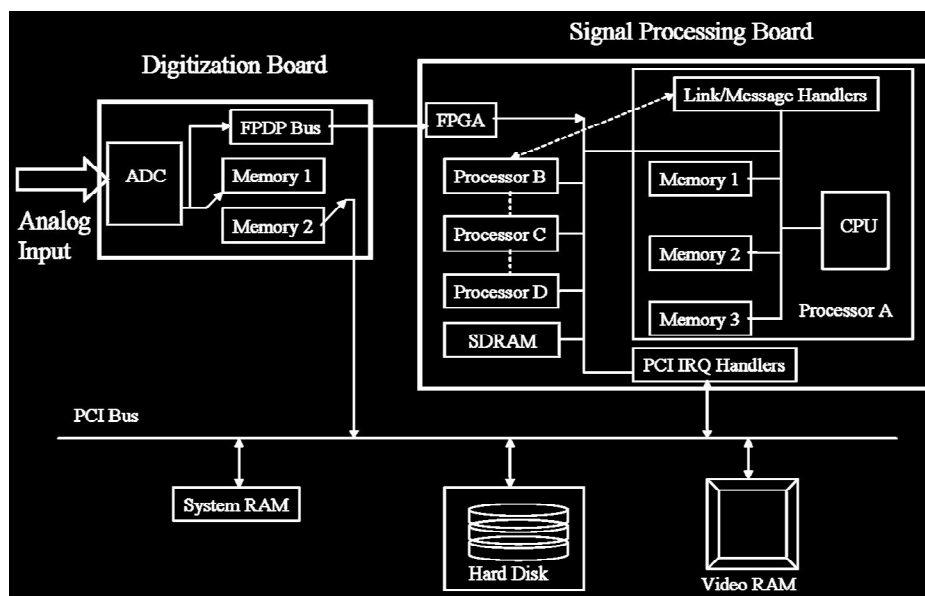


Fig 3.6 Schematic of a single PC data handling system consisting of a multi-channel digitization board and a signal processing board.

- c. Modifying the FPDP firmware: An attempt was made to modify the Xilinx firmware which controls the FPDP data maps. The code was written in VHDL. When the manufacturers of the DSP board were contacted to implement the change, they quoted

a price which was not economically feasible. Delving into the topic proved that modifying the code is beyond the scope of this research project.

PCI data transfer: The data transfer to the DSP boards via the PCI bus was tried as a last option. The digitized data from the ICS was moved to a temporary location on the system memory. Address of this location was then transferred to the DSP program which would then access the ICS data. There are two important points worth mentioning here. Firstly, all the data from the ICS boards had to be stored on contiguous memory blocks, i.e. no fragmentation of data was allowed. If contiguous allocation is not possible, then data has to be divided into several blocks and multiple iterations of uploads would have to be done. Secondly, there was a cap on the size of the maximum contiguously allocatable memory size. The default contiguous memory size is 256Kbytes. This limit was changed using a system registry as instructed in the TS-Toolset manual to Kbytes. Although the PCI transfer option was significantly slower than the FPDP, this was the only method that worked for transferring data sizes of 4000 samples or more per channel per acquisition. As a result such acquisitions had a minimum TR limit determined by the acquisition window, which was much larger than the FPDP TR limit.

III.2.1.2 Mixing Down to Baseband

The data corresponding to a particular channel is separated out as explained previously and put in buffer allocated in the internal memory for faster I/O access (Fig 3.7). Two buffers of the same size as the data size buffer were defined which contained the sine and the cosine values at the digitized IF frequency. Mathematically they were defined as:

$$\sin(n) = \sin \frac{2\pi f n}{f_s} \quad [3.3]$$

$$\cos(n) = \cos \frac{2\pi f n}{f_s} \quad [3.4]$$

Where n is the sampling instant, f is the IF frequency of 500KHz, and f_s is the sampling frequency of 2.5MHz. For data sizes of 3200 per sampling instant and less, the memory for the sine and cosine buffers were allocated in the processor memory and for larger data

sizes the memory was allocated on the SDRAM. The two product buffers were also allocated either on-chip or on SDRAM depending on the size of the data. The product of the data with the sine function becomes the in-phase and the product with the cosine is the quadrature phase signal. Mixing the signal with a 500KHz results in two frequency bands, one centered at baseband and the other centered at 1MHz (Fig 3.8). In order to extract the baseband information, both the product signals are digital low-pass filtered using a finite impulse response (FIR) filter.

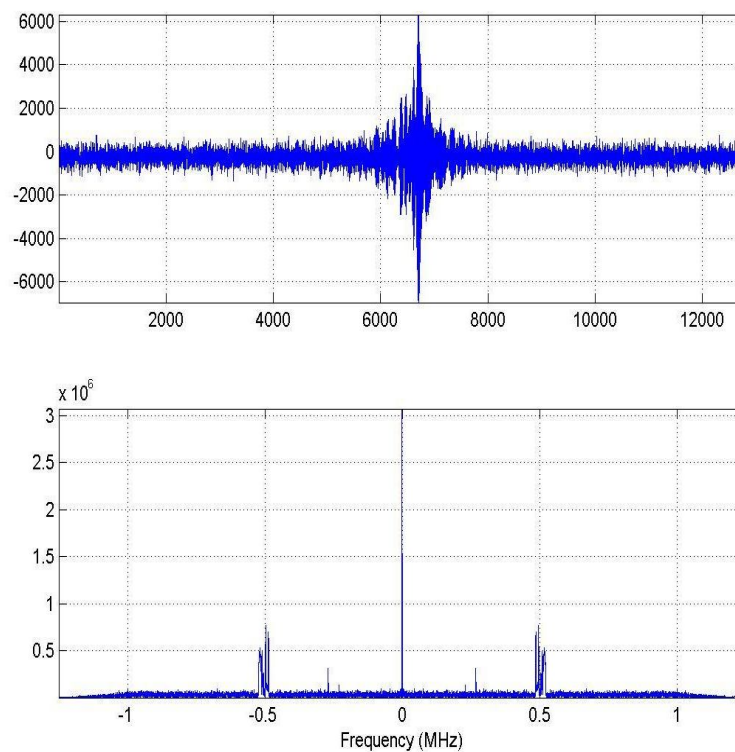


Fig 3.7 Echo data obtained from channel 47 from one of the experiments. An echo centered at IF 500KHz with 50kHz bandwidth and 256 frequency encodes (5.12 ms acquisition window) was digitized at 2.5MHz, which translated to 12800 samples per channel. Also shown along with echo is its fourier spectrum.

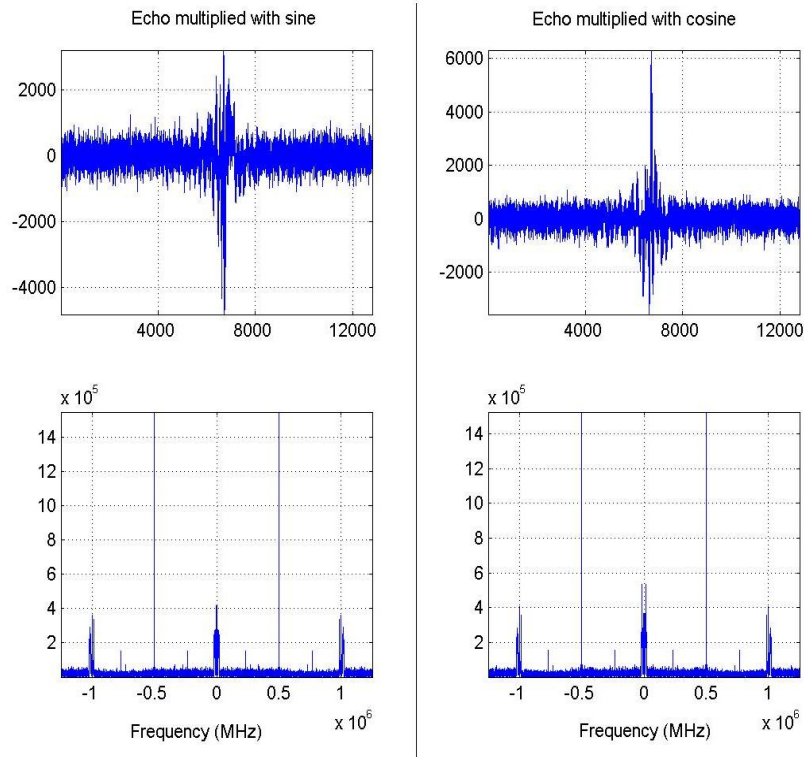


Fig 3.8 Results of the echo after multiplying with sine and cosine functions. The sinusoidal functions are at the IF frequency of 500KHz. The product from the sine function is the Inphase signal and the other product is quadrature phase (referred to as the Q-phase) signal. The fourier spectra shows two bands, one at baseband and the other at the upper sideband of 1MHz.

III.2.1.3 Low Pass Filtering

The coefficients of the FIR filter were determined using the ‘remezord’ algorithm in MATLAB (70). The function takes the following arguments to generate the coefficients: a) a vector of cutoff frequencies (lying in between 0 and $f_s/2$), b) a vector of amplitudes of the cutoff frequencies c) the passband and the stopband ripples, and d) the sampling frequency, f_s . Once the coefficients were determined by the MATLAB algorithm, they were copied into the DSP’s c-code (Fig 3.9) . The array containing the coefficients was declared in the internal memory space of the processor. A linear convolution was performed between the FIR coefficients and the in-phase and the quadrature phase arrays.

$$\text{Filtered_Inphase}(m) = \sum_{k=-\infty}^{k=\infty} \text{Inphase}(k)b(m-k) \quad [3.5]$$

$$\text{Filtered_Qphase}(m) = \sum_{k=-\infty}^{k=\infty} \text{Qphase}(k)b(m-k) \quad [3.6]$$

Where Inphase and the Qphase are the products of the signal with the sine and cosine functions, b is an array of filter coefficients, m is the number of sampled data points, n is the number of filter coefficients. The resultant filtered signal is a baseband signal of length n+m-1 points (Fig 3.10).

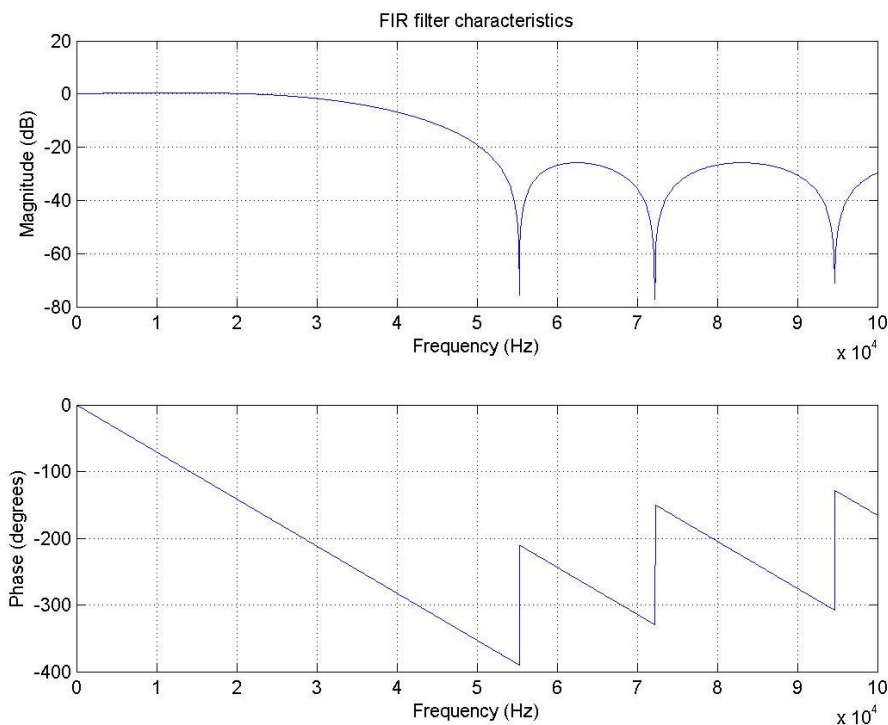


Fig 3.9 FIR filter characteristics showing the magnitude and the phase responses.

III.2.1.4 Convolution Challenges

The challenge faced here was the time taken for computation. Despite limiting the memory usage, keeping the variables to a minimum, allocating as many frequently used variables to on-chip memory locations, the algorithm could not be made to execute at 125 frames per second processing speeds. Investigating the bottlenecks in the procedure:

- a) FPDP data separation into individual channels could not have been made faster. The compiler could not allocate 2 byte integers, hence this avenue was ruled out.
- b) The multiplication of channel data with the sine and cosine functions was done using a library function, surprisingly this option proved slower than regular multiplication.
- c) The convolution algorithm was also tried to with a library function, but regular formula implementation proved much faster. However with thousands of multiplication and addition operations, this operation consumed a large portion of computation time.

After considering the bottlenecks in the process, it was clear that the only way to reduce down the long computation time was to cut down the number of arithmetic operations in the convolution operation. The fact that after the convolution, the signal undergoes a decimation hints that the convolution sum need not be computed at every sampling instant. This led to the idea of decimation within the convolution operation. Hence the 'selective convolution' formula now changes to the following.

III.2.1.5 Decimation

At this center frequency, there are more number of samples than needed to satisfy the Nyquist criterion. This extra information was removed via a process called Decimation. The decimation factor was decided by the equation 3.5. The decimation factor for the example discussed amounts to $3200/128 = 25$. The resultant two decimated signals correspond to the real and imaginary parts of the k-space line represented by the particular channel (Fig 3.11). The real and the imaginary parts of k-space data were obtained by the Equations 3.6 and 3.7 respectively.

$$\text{Decimation_Factor} = \text{Number of digitized samples} / \text{Number of frequency encodes} \quad [3.5]$$

$$\text{Kspace_Real}(k) = \text{Filtered_Inphase}(k * \text{Decimation_Factor}) \quad [3.6]$$

$$\text{Kspace_Imag}(k) = \text{Filtered_Qphase}(k * \text{Decimation_Factor}) \quad [3.7]$$

The process of mixing signals to baseband, FIR convolution and decimation was done after extracting the channel's samples from the FPDP data pool, for all the 32 channels. The algorithm was executed simultaneously on the second set of digitizer and DSP boards. The processed data from each channel was 1-D FFT-ed to get the image profile of the object. The profiles from all channels were combined to obtain the image space (Fig 3.12).

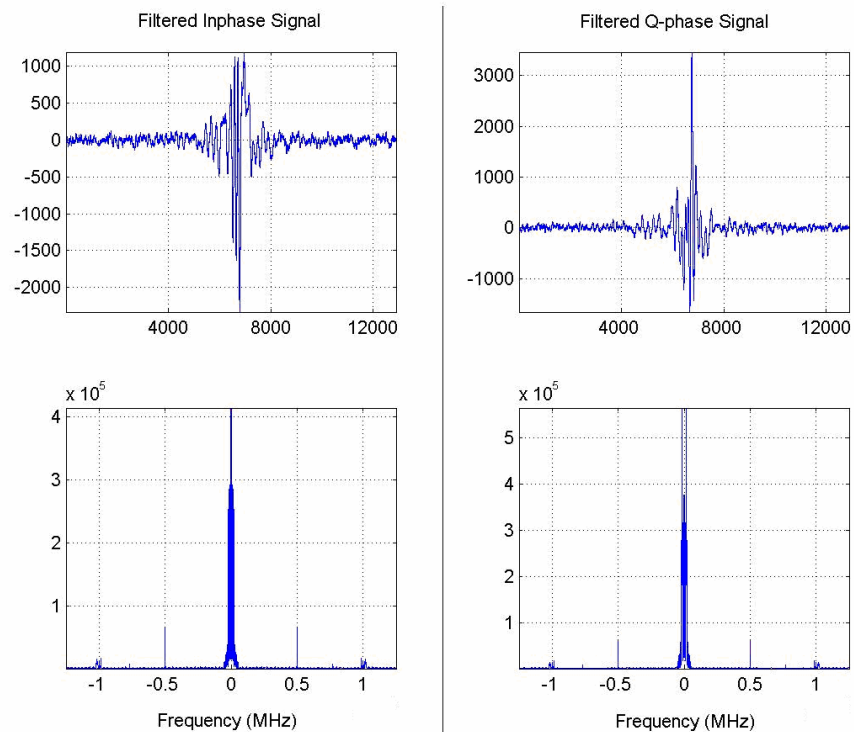


Fig 3.10 Shown are the Inphase and the Qphase signals after removing the upper sideband by convolving with a low pass FIR filter. The fourier spectra shows a single band centered at zero frequency.

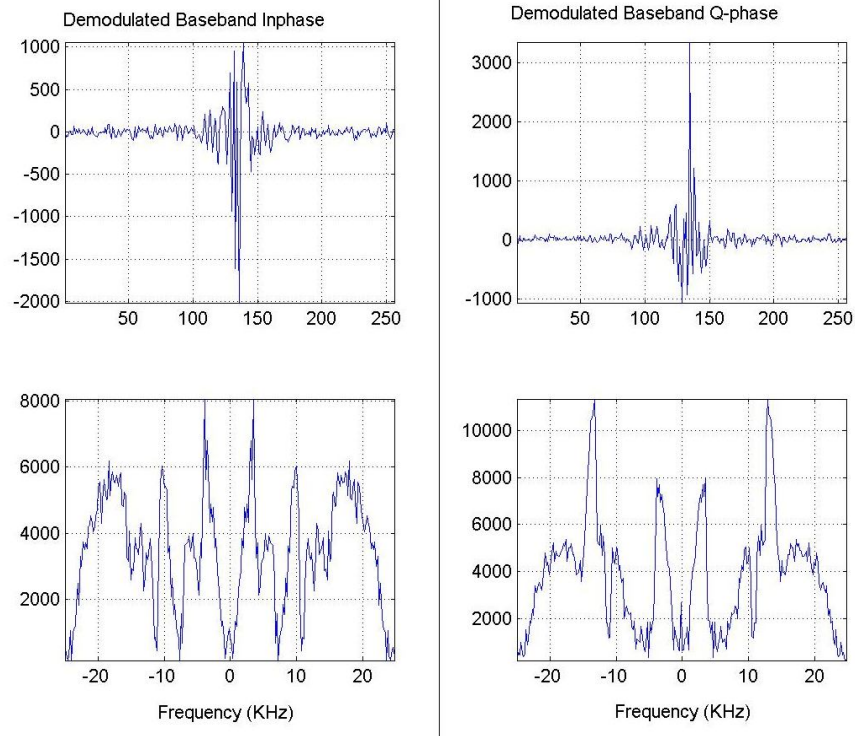


Fig 3.11 Shown are the Inphase and the Qphase signals after removing the upper sideband by convolving with a low pass FIR filter. The fourier spectra shows a single band centered at zero frequency.

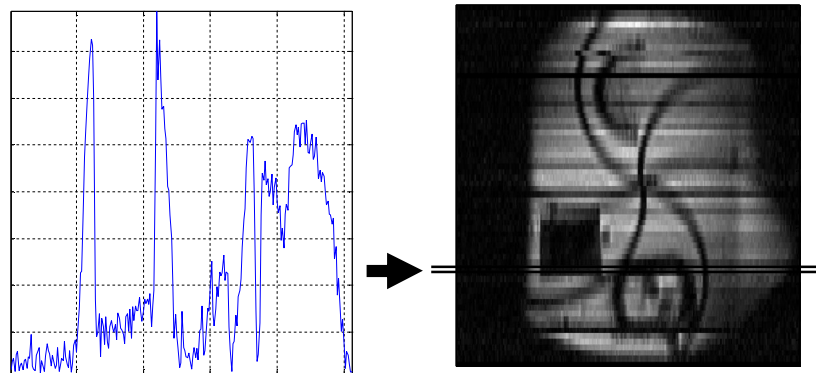


Fig 3.12 The processed data from each channel is 1-D FFT-ed to yield of the profile of the imaging object. The profiles from all the channels are stacked one above the other to form the full image. Shown is the profile of channel 47 and the full SEA image.

There were two places where the fully processed data corresponding to each image could be stored :

- a) In the on-board SDRAM: The SDRAM present on the DSP board has a capacity of 256 Mbytes and a typical 128x64 SEA image occupies 64Kbytes in total or 32Kbytes on each board. This translates to a maximum of 8192 acquisitions before all the data needs to be downloaded into the host computer's hard disk. The option of saving data on the SDRAM is chosen when the experiment demands a very short TR and the time interval isn't sufficient enough to offload the data after every acquisition.
- b) In the host computer's hard disk: The option of storing the data on the hard disk is made when there are more number of acquisitions than the SDRAM can possible store. Also this option requires that the TR be sufficiently long enough for the DMA to occur via the PCI bus to the host computer's hard disk.

III.3 Other Challenges

Spikes in the digitized data: The data digitized by the ICS-645 displayed large amounts of spikes (Fig 3.13). The spikes were because of the digitization and they are not present in the actual signal. Some channels from both the boards would generate huge spikes while other channels would not. The reason for this was not clearly understood. The following tests were done in order to investigate the reason for the appearance of spikes:

1. Master-Slave and Master-Master board configuration: Different configurations of the two ICS-645 boards were tested. The boards were connected in master-master and master-slave configurations. While on-board is master and the other is slave, the trigger and clock was supplied only to the master board which would communicate their information to the slave board via a P4 cable. None of these configurations really eliminated the spikes from the data. To eliminate the possibility of a hardware design flaw, loan boards were ordered from the manufacturer while the existing boards were sent for repair. The loan boards although of a totally new design, in the master-master configuration showed no spikes. But this was not repeatable with the existing boards even after they were returned from repair.
2. Changing the sampling frequency: The manufacturer's engineers expressed concern that the clock supplied to the boards may not be perfect TTL signal and this could lead to spikes in the data. The clock that was supplied to the digitizer boards was a

40MHz clock. For the lack of an alternate supply, a 20MHz clock supplied by an SRS function generator was used. A 20 MHz clock meant that the sampling would now be at 1.25MHz per channel than the 2.5MHz initially used. Interestingly enough, there were no spikes that were noticed. Hence the spikes were attributed to ill-conditioned clock signal. The 20MHz clock signal was better conditioned than the 40MHz one. To avoid the spikes in the data, the sampling was continued at 1.25MHz.

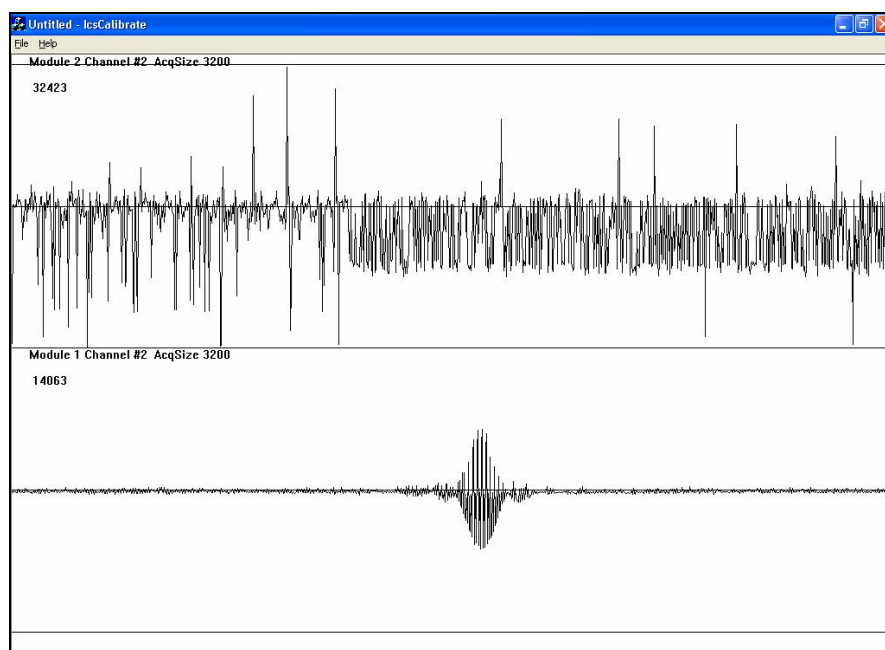


Fig 3.13 Digitized data from two of the 64 channels is shown, one from each of the ICS-645 boards. The digitization process introduced a large amount of spikes in the data in some channels. The occurrence of the spikes only in a few channels and not in all was not understood until tests were carried out.

Reducing the sampling frequency however raised the issue of SNR degradation. At lower sampling rates, the noise was expected to alias resulting in lower SNRs. To investigate this concern and quantify the changes, images were made with 2.5MHz, 1.875MHz and 1.25MHz sampling rates. A single channel in-house birdcage coil was used to collect the data. An SNR phantom consisting of two test tubes containing different CuSO_4 concentrations was used. The data was processed through one of the channels of the 64 channel receiver and sampled using the 40MHz clock (2.5MHz per channel). The process was repeated with the SRS clock at 30MHz (1.875MHz per

channel) and 20MHz (1.25MHz per channel). The digitized data was processed as described in the previous sections. The SNR of the images was computed by picking two regions of interest in one each in the signal and noise areas and taking ratio of their summed pixel intensities (Fig 3.14). The SNR values were also compared to the one obtained from the Omega scanner console (Table 3.1)

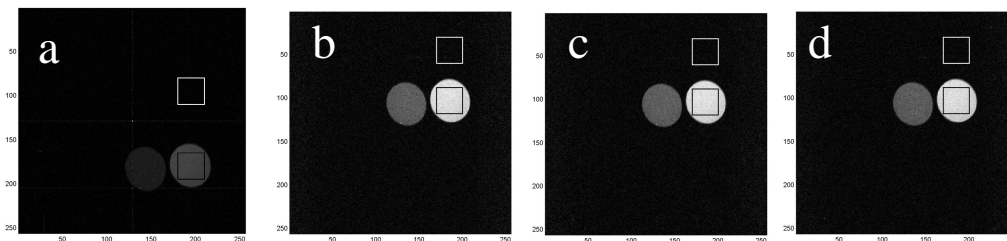


Fig 3.14 Shown are the images (from right to left) reconstructed from the console (a) and images reconstructed from data sampled at 2.5MHz (b), 1.875MHz (c) and 1.25MHz (d) respectively. The regions of interest used to compute the signal and the noise intensities are shown in the rectangular boxes.

Table 3.1 A comparison of the SNR values obtained from images sampled at three different sampling rates and the console reconstruction

Fig	Sampling Rate (per channel)	SNR
3.14a	2.5MHz	18.83
3.14b	1.875MHz	20.04
3.14c	1.25MHz	20.02
3.14d	Console reconstructed	14.02

Surprisingly the SNR did not go down with sampling rate as was expected. The reason for this strange behavior was not evident until later in the research. Chapter IV discusses this in detail. After the SNR tests, the sampling frequency was changed from 2.5MHz to 1.25MHz. for all subsequent imaging experiments. This did reduce the data generated by half and shortened the processing time. The minimum TR for fast imaging reduced from 8ms to 5ms. At 200 frames per second we had built one of the fastest parallel MRI reconstruction system in the world.

- a) Unreliable DMA to host computer's hard disk: An interesting problem occurred during experiments with very large number of acquisitions. It was observed that after a couple of thousand acquisitions, the host computer would 'miss' one or two acquisitions. For example if the host computer was programmed to acquire 8192 acquisitions, it would only acquire 8191 or 8190. The happening of this event was not clearly understood. To solve this problem, experiments with significantly large TR values (like a couple of seconds) were conducted, thinking that the demodulation process was taking longer time. Even in such cases, there were missing acquisitions. So, it was not the algorithm. We tried replacing the hard disk, the motherboard, processor and even the memory on the computer, but to avail. The acquisitions were repeated with the digitizer boards seated in an old motherboard which originally housed them (when the DSP boards were purchased, we upgraded the system). This experiment went smoothly and the programmed number of acquisitions were acquired. The only difference between the new and the old systems was the format of the file system on the hard disk. For reasons beyond the scope of this research project, a hard disk formatted under the FAT32 format is more reliable compared to an NTFS formatted hard drive.

III.4 Symphony Software Setup

A user friendly, GUI based software, 'Symphony' was written to control the digitizer, DSP boards and the various algorithms. The software was written in Visual C++ language using the Microsoft Foundation Classes (MFC) via the VC++ 6.0 package (Microsoft corp., Redmond, WA). Developing the software in VC++6.0 was an obvious choice given the fact the drivers, libraries and compilers for the digitizer and the DSP boards provided by the manufacturers were developed for the C environment. The software evolved from a basic command line win32 application to the current GUI based version, with atleast 6-7 revisions over the period of time.

One of the first pieces of software that was written was to visualize the digitized data. This was needed to calibrate the echoes by adjusting the variable gain and the attenuator control knobs going into the 64 channel mixers. Initially the number of samples that were

displayed on the screen was hard-coded to 3200, 6400 and so on. But as the sophistication of the software grew over time, this was replaced by a variable quantity. calibration software for the ICS data. The following is a step-by-step procedure followed in an imaging experiment.

1. Choosing the settings:

The following are the various fields under the settings menu (Fig 3.15):

- a. Spectral width of the signal (default at 50KHz)
- b. Number of frequency encodes (default at 256)
- c. Sampling rate (default is 1.25MHz)
- d. Board Config (default is Master-Master): If using under master-slave configuration, P4 cable is needed to connect the two ICS boards.
- e. Trigger (default is external)
- f. Clock (default is external)

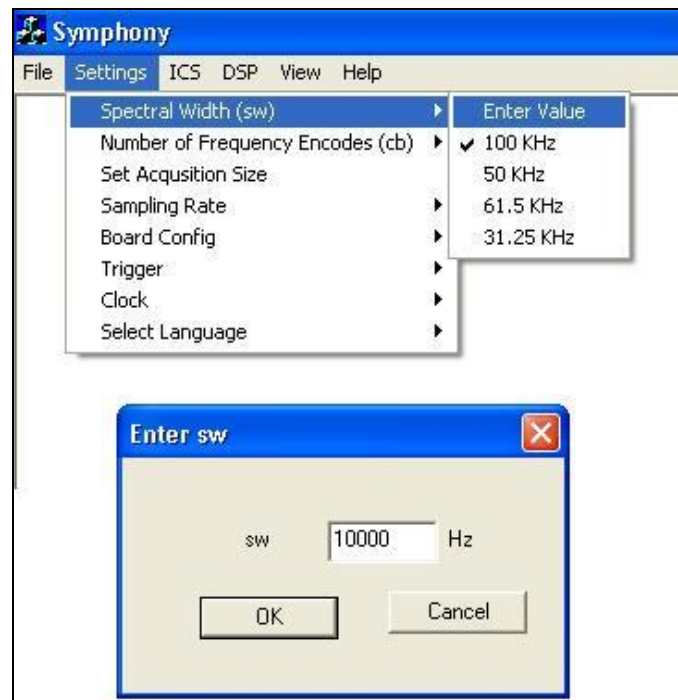


Fig 3.15 The settings menu with the imaging variables.

2. Digitization only using the ICS boards:

The setting would now be programmed on to the digitizer boards and the boards wait for the trigger from the console to start digitization (Fig 3.16). Only digitization is done here. The fields under this tab are:

- a. IcsReset: Resets the ICS boards
- b. IcsConfigure: Configures the board with the settings chosen in the previous step.
- c. IcsCalibrate: Displays the digitized data in real-time facilitating the calibration of variable gain and attenuator settings.
- d. IcsAcquire: Executes a win32 application which digitizes the data and stores as .ics files.
- e. IcsDemodulate: Reads from the hard disk previously digitized data in the .ics format and demodulates into .dsp files.



Fig 3.16 The ICS menu with various fields.

3. Digitization and demodulation using the ICS and the DSP boards:

This tab is chosen to digitize as well demodulate the data using the DSP boards (Fig 3.17). The demodulation algorithm discussed in the previous sections of the chapter is implemented on the DSP boards. The fields under this tab are:

- a. DspReset: Resets both the DSP boards
- b. DspAcquire: This win32 executable first programs the ICS boards with the imaging parameters and then implements the DSP algorithm. As a part of the implementation, the boards are initialized, loaded with Xilinx firmware and then pre-compiled .dxe (DSP executable) files are loaded on the TigerSharc processors for demodulation and decimation.

However there was a problem here. The filter coefficients which were used to low pass filter the baseband signal, were calculated using a MATLAB algorithm. This meant that the filtering process could not be carried out for any arbitrary bandwidth signal. So, DSP files for a large number of bandwidths commonly used for imaging were precompiled. Hard-coding the filter coefficients for only certain number of bandwidths undermined the versatility of the software. To overcome this problem, an executable of the `remezord` algorithm was created in MATLAB commands and copied to the 'Symphony' structure. This allowed generating filter coefficients for filtering any bandwidth signal.



Fig 3.17 The DSP menu.

The issue of demodulating any bandwidth signal was not completely resolved yet. Even though having a generator which would provide coefficients, these coefficients could not be loaded on the DSP during run-time. The compiler supplied by the manufacturer did not allow allocating memory spaces during run-time which was very imperative to load any arbitrary length filter coefficients.

The problem was solved by writing a code which generated a DSP C code with the supplied filter coefficients, compiled it and loaded the `.dxe` file on the DSP, all during run-time. The code to generate the DSP code is part of the Symphony program. This facilitated filtering any arbitrary bandwidth signal.

4. Viewing the data:

This tab provides the user to visualize of the previously processed data and also view data in real-time. The opportunity to view SEA images in real-time really save time when optimizing parameters such as RF power, gain, phase compensation gradient, slice offset, and other imaging parameters.

This chapter provided an in-depth description of the SEA image reconstruction system. To test the performance of the system, it was used to image rotating phantoms at 200 frames per second(45,71), measure turbulent flow patterns(72), MR microscopy(73) and other applications. One of the applications with this tool, the study of shear modulus during thermal ablation in an agarose phantom using MR Elastography will be covered in detail in chapter V. In the following chapter, a new method to reduce digitized data is presented. The new method is very useful in data intensive applications such as MR microscopy.

CHAPTER IV

IMPROVEMENTS IN DATA HANDLING ISSUES BY REDUCED SAMPLING RATE METHOD

As discussed in the previous chapters, a significant problem in MRI systems with a large number of receiver channels is the amount of data that is generated and needs to be processed. Emerging technologies in parallel Magnetic Resonance Imaging (MRI) with massive receiver arrays are increasingly becoming popular in clinical and research practice. On the clinical side, parallel MRI techniques such as whole-body imaging, real-time cardiac imaging, catheter tracking, and MR-guided surgical procedures have become valuable tools for a physician's assessment and treatment of various pathologies (33,35-48). Parallel imaging has also made possible for researchers to explore exciting new avenues where MRI is being used to investigate high temporal resolution rapid flow imaging, MR Elastography and high resolution MR microscopy (36,45,73,74). As the number of channels employed for parallel MRI grew to 32, 64 and even 96, there was need to process the large amounts of data quickly while maintaining high signal fidelity (28,38,51-55,75). To avoid 'ghosting' of the data which was one of the major disadvantages of the analog quadrature mixers, digital receiver technologies were introduced consisting of very high speed Analog to Digital Converters (ADCs) along with digital FIR filters and high performance Digital Down Converters (DDCs) (34,49,50,56-60). Although these methods solved the problem, they were not economically feasible on commercial MRI systems as well as on research scanners equipped with a large number of coil arrays, with some of the standard designs costing \$10,000 per channel and upwards (34,76-78).

While an increasing number of receiver channels not only implies higher costs, it also translated to a corresponding increase in the amount of data being generated and processed, slowing down the process of image reconstruction. This problem is further aggravated by the fact that most, if not all, multiple channel receiver systems use digital demodulation with digitization at an Intermediate Frequency (IF) (34,61,79). Our in-house developed 64 channel system was designed to mix down to an IF frequency of 500 KHz, where each channel was sampled at 2.5 MHz per channel, with a 1MHz anti-

aliasing filter built into each receiver channel to prevent noise filtering (61). This design led immediately to limitations in the maximum sampling time as the digitizer memory filled up, and in TR, due to data transfer rates.

A common approach is to use IF undersampling techniques, which was investigated by our group (80). To be most efficient, IF undersampling technique for variable bandwidth sequences would have required active tunable band-pass filters on each channel and the cost of procuring these filters proved to be economically prohibitive. Commercially available tunable filters operating at IF specifications for a 64 channel system are not only very bulky but also can cost up to \$90,000 (81). An alternative approach, mixing to a lower frequency would require 64 variable cutoff low-pass filters. However, modern multiplexing high-speed digitizers are now implementing digital anti-aliasing filters (66).

This paper describes the use of a variable IF frequency, combined with an analog low-pass filter and the digital anti-aliasing filters to drastically reduce data handling requirements without any hardware modifications to our previous system design. Many low-cost ADC's in the past did not have the anti-aliasing filters. For example, chips such as the Analog Devices AD6645 offers digitization of up to 200MHz but without any anti-aliasing filter (82). These results should be of interest to researchers implementing IF sampling receivers.

IV.1 Materials and Methods

Hardware Setup

The 64 channel receiver used for these experiments was built using 64 single conversion receivers assembled from widely available discrete circuits, mainly from Mini-Circuits (Mini-Circuits, Brooklyn, NY) (61). The single stage mixing results in an IF that can be anywhere from 1MHz to near baseband. In all previous work, an IF frequency of 500 KHz was chosen to support up to 500 KHz spectral width sequences within the 1 MHz anti-aliasing filter. Two 32 channel digitizer boards, ICS-645, were used for the process of digitizing the IF signal (66). Each board is a 33MHz 32-bit PCI card capable of

sampling at the rate 2.5MHz/channel generating 16 bits per sample. Each channel was digitized at 1.25 MHz sampling rate, yielding a data rate of 160 MB/second, which exceeded the practical PCI bandwidth. For this reason, the data is passed to a DSP board, TS-P36N, for digital demodulation using a fast FPDP bus (69). A schematic and a picture of the setup is shown in figures 3.3 and 3.2.

However, the DMA, data buffering rates and the memory capacity on the DSP board limited the TR to 5ms at 100KHz bandwidth signals. The TR limit for signals with lower bandwidths was much higher. Alternatively, the memory specifications on the digitizer board limited the acquisition to 13.26ms when all the 64 channels were used. These limited the performance of the 64 channel system for a wide-range of real-time applications involving higher resolution but also in data intensive applications such as MR microscopy. IF undersampling at 500 KHz would eliminate this problem, but the band-pass filters centered at 500 KHz were cost prohibitive. An alternative approach was simply to reduce the clock rate and lower the IF frequency. However, it was felt that this would require anti-aliasing filters as conventionally used in MRI receivers. Such filters are not found on most dedicated ADC chips. The Analog Devices AD9260 chip found in the ICS-645 does provide anti-aliasing through built-in DSP (82). The chip provides a noise band from one-half Nyquist rate to 7.5 times the Nyquist rate. As long as the stop band is within the fixed analog anti-aliasing filter, the sampling rate can be decreased as needed.

IV.2 Results

In order to verify the algorithm and test the performance of the anti-aliasing filter, experiments were performed with different sampling frequencies. An echo with 50kHz bandwidth, IF 500kHz was digitized at 1.25MHz sampling rate, i.e. 6400 points per channel were obtained using the ICS-645 digitizers. is shown in The echoes from 64 channels were then quadrature demodulated to baseband, decimated to 256 points and 1-D fourier transformed to obtain the Single Echo Acquisition MR image. A block diagram of the process is show in figure 3.4. An echo from one of the channels and its 1-D FFT profile after demodulation and decimation is show in figure 4.1.

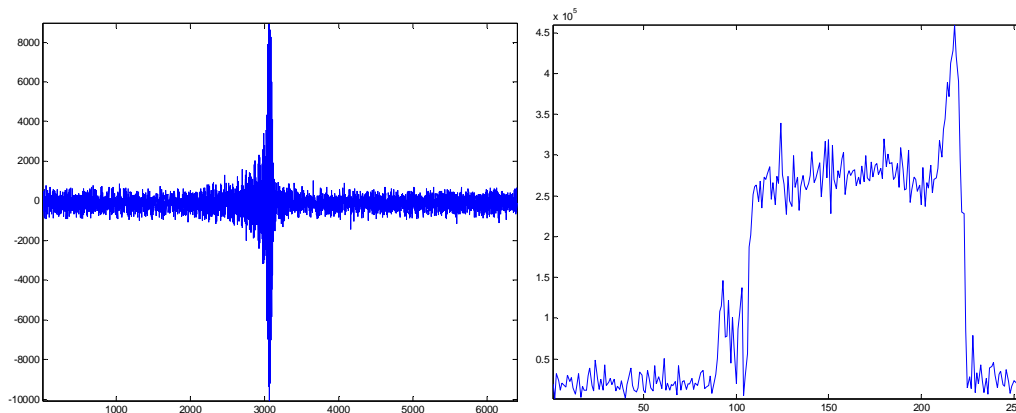


Fig 4.1 Digitized echo at 1.25MHz shown along with its profile after processing.

This experiment was repeated for four more IF and sampling rate configurations listed in Table 4.1. The IF was varied from 500KHz to 100KHz The sampling frequency was varied from 1.25MHz per channel to 250KHz per channel with steps of 250Khz. The IF frequency was controlled by a UnityInova Varian console (Varian Inc., Palo Alto, CA) and the clock to the digitizers was supplied from a function generator SRS DS 345 (Stanford Research Systems, Sunnyvale, CA). The digitized echoes at different sampling frequencies and their profiles are shown in figures 4.2-4.5. The processed images are shown in figures 4.6(a-e).

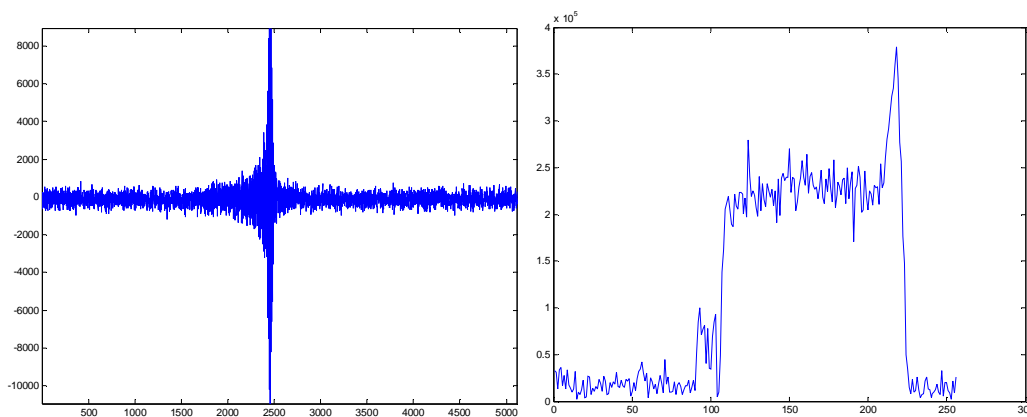


Fig 4.2 Digitized echo at 1MHz shown along with its profile after processing.

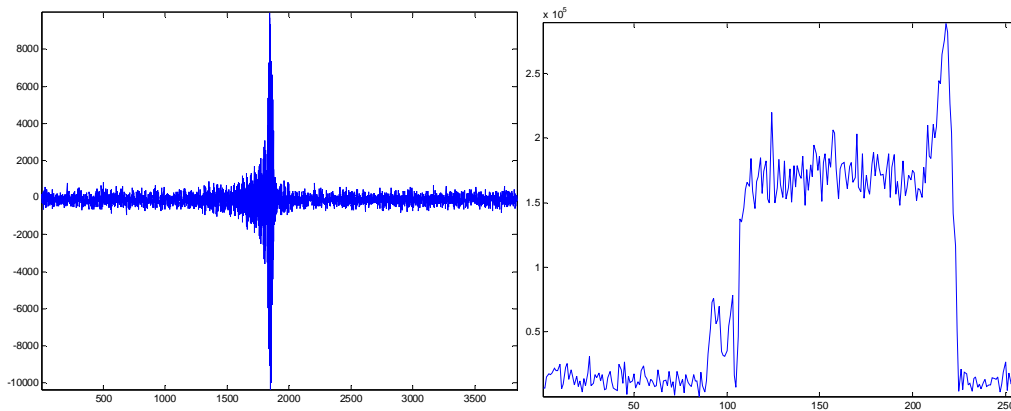


Fig 4.3 Digitized echo at 0.75MHz shown along with its profile after processing.

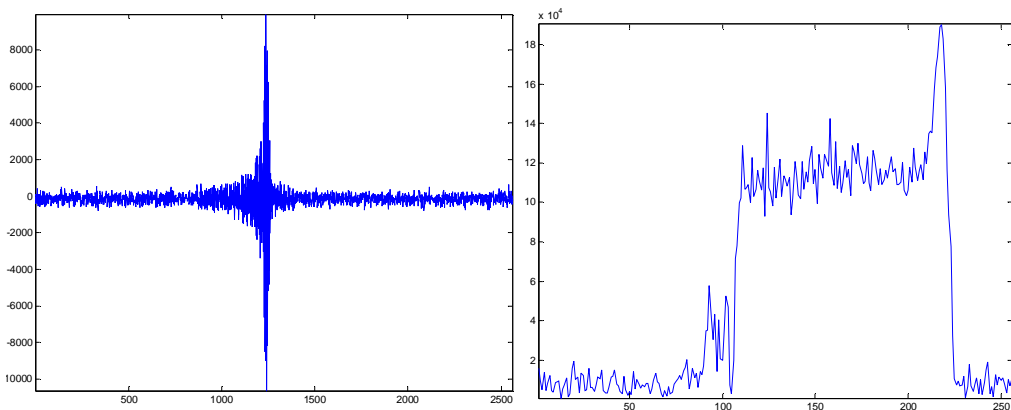


Fig 4.4 Digitized echo at 0.5MHz shown along with its profile after processing.

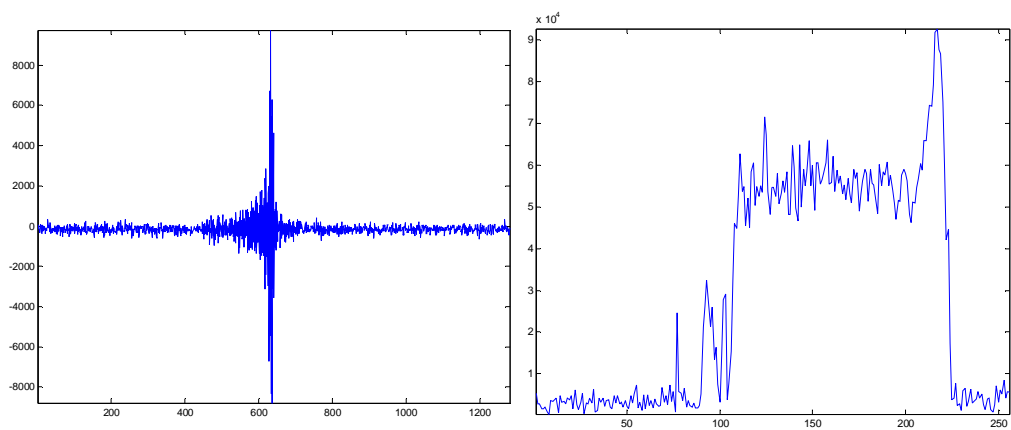
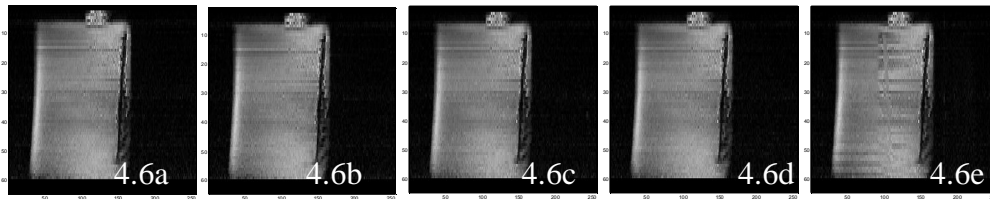


Fig 4.5 Digitized echo at 0.25MHz shown along with its profile after processing.



Figures 4.6(a-e) Shown are SEA images reconstructed by varying IF and sampling rates for 5 different configurations. The details of the configurations are listed in Table 4.1.

Table 4.1 SNR comparison of the images obtained at 5 different sampling rates

Fig#	IF (kHz)	Sampling freq (MHz)	SNR
4.6a	500	1.25	10.55
4.6b	400	1.00	10.76
4.6c	300	0.75	10.36
4.6d	200	0.50	10.75
4.6e	100	0.25	10.55

The SNR computed for the all the five sampling configurations measure the same. This is explained by the inherent anti-aliasing feature of the ADC chip. The amount of data generated as the sampling rate changed from 1.25MHz to 250KHz reduced by a factor of 5. This means that a 2048x2048x64x32 MR microscopy data set would now generate 3.2 GB instead of the usual 16GB. Also, reduced amount of digitized data will now allow us to explore 64 channel high resolution MR imaging at higher frame rates.

In order to investigate the lowest sampling rate we could achieve, the frequency response of a receiver channel is calculated using two network analyzers, HP 4195A and HP 4395 (Hewlett Packard Company, Palo Alto, CA). Below are the responses for a -10dbm input, 0Mhz span for center frequencies of 500, 400, 300, 200, 100, 90, 80, 70, 60, 50, 40, 30, 20, 10, 5, 0 KHz.

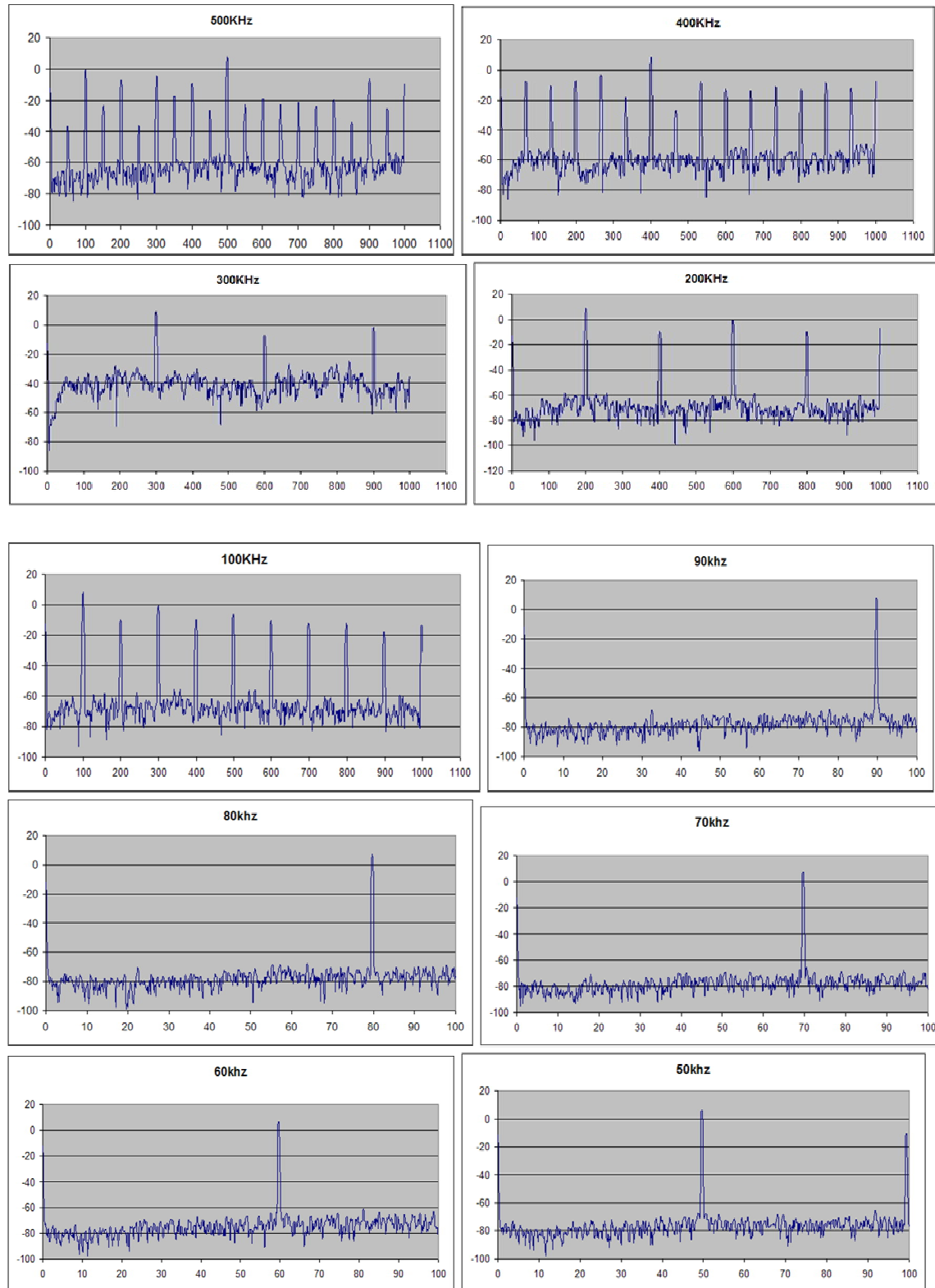


Fig 4.7 Frequency response of one of the 64 channel receivers for a -10dbm input, 0MHz span for center frequencies of 500, 400, 300, 200, 100, 90, 80, 70, 60, 50, 40, 30, 20, 10, 5, 0 KHz.

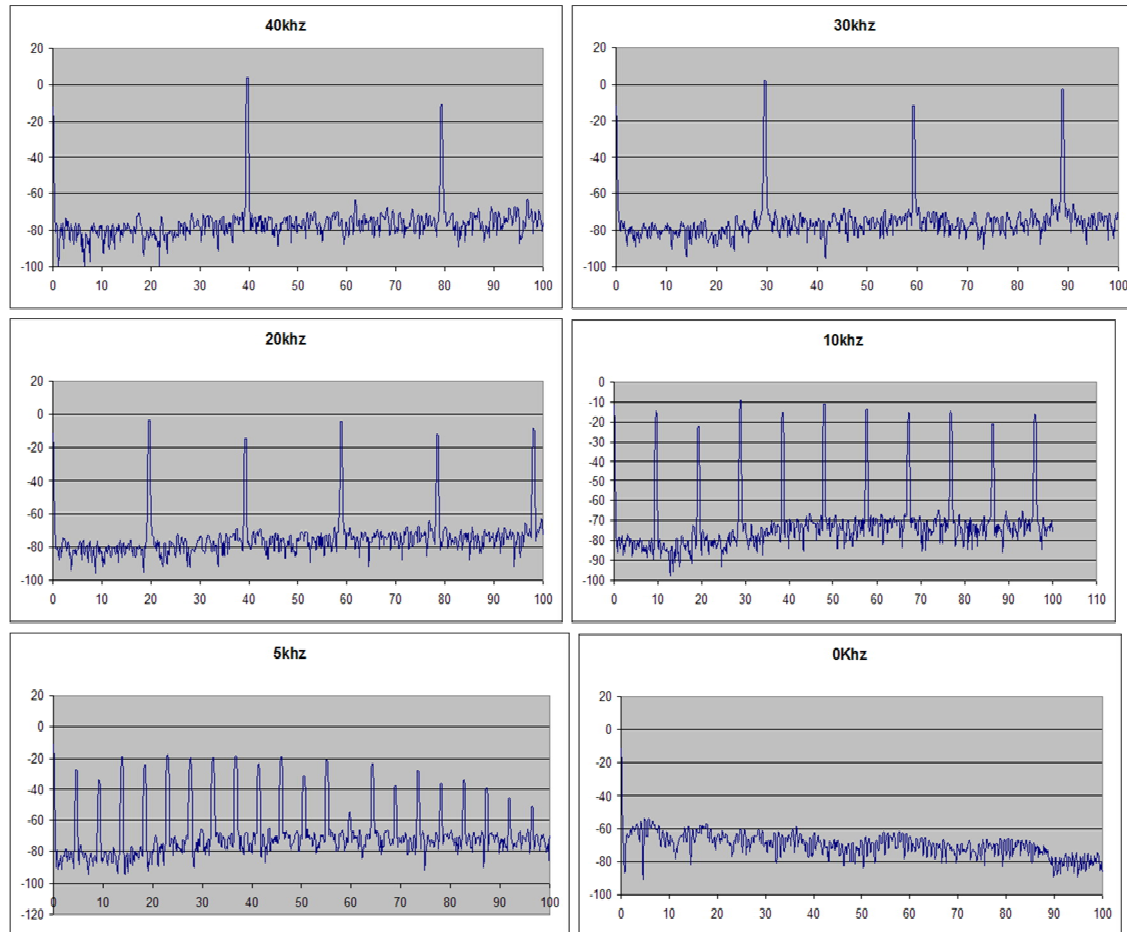


Fig 4.7 Continued.

The frequency response indicates that the performance of the receiver starts to deteriorate for center frequencies below 100KHz (Fig 4.7). Taking into account the bandwidth of the signal, the minimum sampling rate that could be used is 250KHz.

MR receiver technology with increasing number of channels can be expensive and beyond reach for many research groups. The advances in receiver technology have made sampling at increasing higher rates a possibility, with the state-of-the-art digitizers capable of sampling at 2GS/s (83). The issue in this case is the amount of data being generated, which could not only limit the acquisition window but also increase the TR. The proposed solution of using reduced sampling rates, combined with the currently available dual and quad core CPU technologies can bring many research groups a multi-channel real-time reconstruction system within reach.

CHAPTER V

APPLICATIONS TO MAGNETIC RESONANCE ELASTOGRAPHY

This chapter presents one of the most exciting applications of SEA imaging encountered during the course of this research work. Conceptually, the possibility of imaging shear waves using MRI has been demonstrated by various research groups and the diagnostic importance of these measurements has also been shown. But, to use the SEA technology and the reconstruction system to image shear waves and to demonstrate an advantage over the existing MR elastography methods, from an abstract concept to extracting shear stiffness values was a journey full of adventure. The chapter introduces the concept of MRE, its importance, the work that has been done before by other research groups. This is followed by preliminary experiments done using the SEA imaging as a proof of concept, transient imaging and finally applications to estimating shear stiffness values in thermally ablated tissues.

V.1 Magnetic Resonance Elastography and Current Limitations

Magnetic resonance elastography (MRE) is a technique that allows the measurement of shear stiffness in tissues using MRI and acoustic vibrations. MRE offers the ability to obtain stiffness information about tissues in a non-invasive manner, providing information comparable to what a physician learns from palpation in vivo (84-87). Muthupillai and his group's seminal publication in 1995 has shown that using the MRE technique, pathologically valuable elasticity information such as shear modulus distributions in tissues not accessible because of depth or protection can be extracted(84). While this is accomplished at high frame rates using ultrasound, the ability of MRI to access these areas with sensitivity and resolution is superior (88,89). Studies have shown that the shear elastic modulus of tissues are vitally linked to its biological function and pathological condition, increasing the utility of MRE as a diagnostic tool, particularly in the assessment of breast and prostate cancers, liver fibrosis and also in the biomechanical modeling of muscles in sports medicine (90-103).

MR elastograms (image of tissue stiffness) are obtained by exciting the phantom with low frequency acoustic vibrations, this can be either be a transient or by introducing more

periods of harmonic vibration into tissue (84,104) . For harmonic and steady state MRE, a single image with phase encoding stepped in synchronization with the applied harmonic vibration enables the propagating or standing acoustic wave to be visualized using motion encoding gradients. The propagation of the acoustic wave in the tissue is studied by varying the time lag between the start of the acoustic exciter and the motion encoding gradients. However, there is increasing interest in visualizing transient effects. When applying a mechanical transient, many temporal offsets are required to capture the propagation of vibration in the tissue, resulting in long acquisition times as each “frame” in the elastogram movie requires the acquisition of a complete image.

Several research groups have proposed techniques for rapid acquisition of MRE data. Glaser et al showed that the scan times in MRE experiments can be reduced by a factor of 8 using reduced FOV and by a factor of 64 using 1-D MRE (105). Using a modified version of the SPAMM sequence, Lewa and group have demonstrated MRE of unknown excitation frequency and also reduced the acquisition time to a few seconds (106). Yuan et al, have demonstrated a reduction in imaging time doing a 1-D MRE (107). Multi-echo phase contrast sequences have also shown to lessen the MRE imaging time (108). Despite these advances, the acquisition time for a full image takes the order of a few seconds.

Reduction in imaging time during MRE experiments was desired to observe dynamically changing tissue properties. Although the agents that bring about this change in tissue properties are not stated at this point, it was nevertheless decided to demonstrate the advantage of SEA imaging in reducing MRE scan time.

V.2 MRE of Agarose Gel During Thermal Ablation

Information on dynamically changing tissue material properties during thermal ablation gives insight into their dependency on temperature change. This is particularly of great interest in the treatment of tumors via tissue ablation therapies such as focused ultrasound (FUS), where an important part of the ablation treatment is to estimate the spatial extent of tissue coagulation (109-114). The use of magnetic resonance elastography (MRE) techniques in determining the thermal dose needed in ablation therapies by measuring

temperature sensitive tissue shear modulus has recently been established (115,116). The MRE images of ablated tissues promise to have higher contrast and provide a quantitative measure of tissue damage when compared to conventional MR estimates of temperature dependent parameters such as T1 relaxation time, chemical shift as well as the T2-weighted images (115-118). However these MRE images are not instantaneous ‘snapshots’ of the tissue material properties since they are acquired over a period of a few seconds, even using the rapid MRE techniques developed (105-108). The following research work presents that by completely eliminating phase encoding, using the single echo acquisition (SEA) MRI, high temporal resolution movies of shear modulus changes in tissues can be obtained for a better understanding of dynamically changing tissue properties and hence improved FUS therapies.

V.2.1 Materials and Methods

64-channel Single Echo Acquisition System

The 64 channel SEA coil in conjunction with the 64 channel receiver array and reconstruction system was used for receiving and demodulating the MR signal (65,71,75). A volume coil, constructed in house, was used for RF transmission. The setup was integrated into a Varian UnityInova console (Varian Inc., Palo Alto, CA) and a 4.7T/33cm Oxford magnet (Oxford Instruments, Oxford, UK). A phantom measuring 10.3cm x 7.5cm x 0.75 cm was constructed with 0.1 g/L CuSO₄ and 0.9 grams of agarose gel for the study.

Thermal Ablation System and Sonic Vibrations

The thermal energy to heat the gel was derived from a commercially available 50W/12V GE halogen bulb (GE Consumer and Industrial, Cleveland, OH), connected in series to two 1ohm non-inductive Dale NH250 resistors (Vishay Intertechnology, Inc., Malvern, PA) and a Tripp-Lite PR-7b 12 V DC power supply unit (Tripp Lite, Chicago, IL). The resistors were needed to reduce the current flowing in the bulb, which meant reduced force due to magnetic fields and increased longevity. Reduced current in the circuit meant

that the bulb acted like a 17.42 W constant heat source. The bulb was held at 1 cm above the surface of the gel using a mechanical fixture.

Audio frequency vibrations were created in the gel phantom by using a solenoid placed in the B_0 field with its axis in the x-direction. When supplied with an alternating current, the solenoid vibrated, creating x-directed shear waves in the gel via a pivoting wooden rod. The rod was connected on one end to the solenoid and the other to a plexiglass vibrating plate in contact with the gel (Fig 5.1). To make sure that vibrating wedge made firm contact with the agarose phantom, the phantom was gelled with the wedge in place (Fig 5.2). 200 Hz sinusoidal waves were supplied to the solenoid by a National Instruments PCI-6713 (National Instruments Corp, Austin, TX) analog output card stepped up using a commercial audio amplifier (RadioShack Corp., Fort Worth, TX).

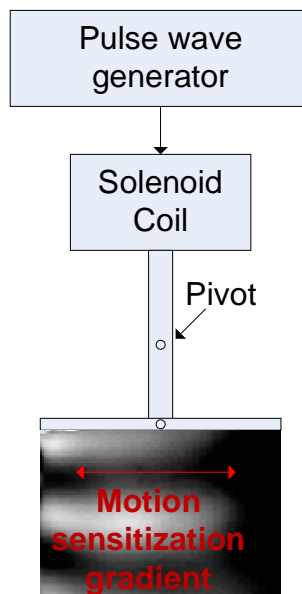


Fig 5.1 The shear waves were generated using a sinusoidal voltage supplied to a solenoid oriented along the x-axis, orthogonal to the B_0 field. A pivoted wooden rod connected to the solenoid on one end and a rectangular plexiglass on the other was used to transfer the sinusoidal motion from the solenoid to the phantom.

The NI output card was controlled by a MATLAB (The Mathworks Inc., Natick, MA) script and triggered by an output from the MRI console. The vibrations were set into motion 10 milliseconds (2 wavelengths) prior to the execution of the pulse sequence (Fig

5.3). This was done to make sure that there were a few shear waves in the gel while encoding the motion while not allowing standing waves due to reflections from the farthest end of the phantom walls. The vibrations were kept on for 30 ms or 6 time periods.

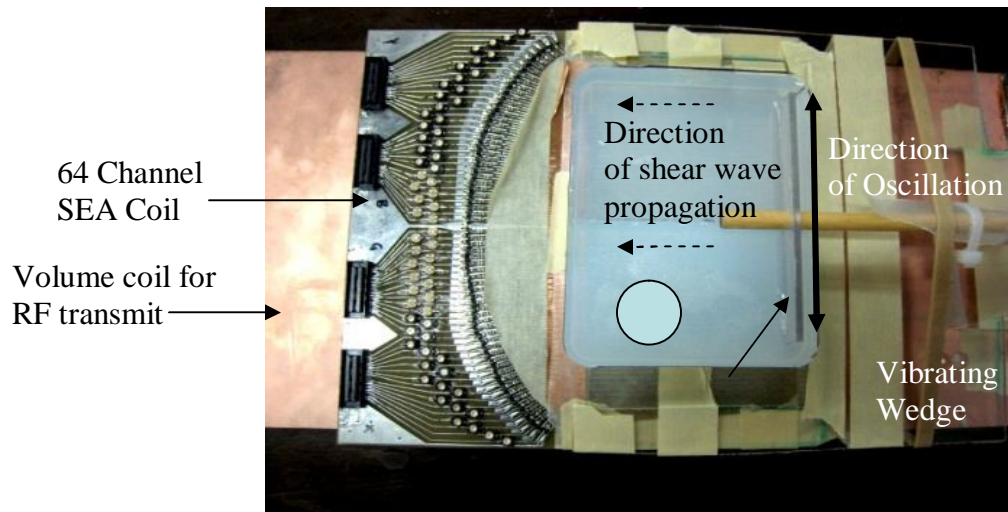


Fig 5.2 The picture shows the transmit volume coil with the top removed, the 64 channel SEA receiver coil, and the agarose gel phantom with the vibrating plexiglass wedge. The plexiglass oscillates at 200Hz along the x-direction, creating shear waves propagating in the z-direction.

Motion Encoding Pulse Sequence

A standard spin echo sequence was modified to include one wavelength of an x-directed 200 Hz sinusoidal motion sensitization gradient. This was followed by an exactly similar sequence with the gradient amplitude polarity reversed. To allow the shear waves from the first sequence to completely attenuate, the second sequence was separated by 500ms. Throughout the positive and the negative motion encoding gradients, the phase encoding gradient was made static to provide phase compensation, necessary for SEA imaging. As the imaging slice is parallel to the array and the coil patterns are highly localized, the 1D FFT of the signal from each channel represents the profile of the gel above each coil. These profiles are combined to form a full image per echo. From a single echo a 256 x 64 coronal SEA image matrix with a 22ms TE and a 160mm FOV was obtained, one each for positive and negative motion encoding gradients.

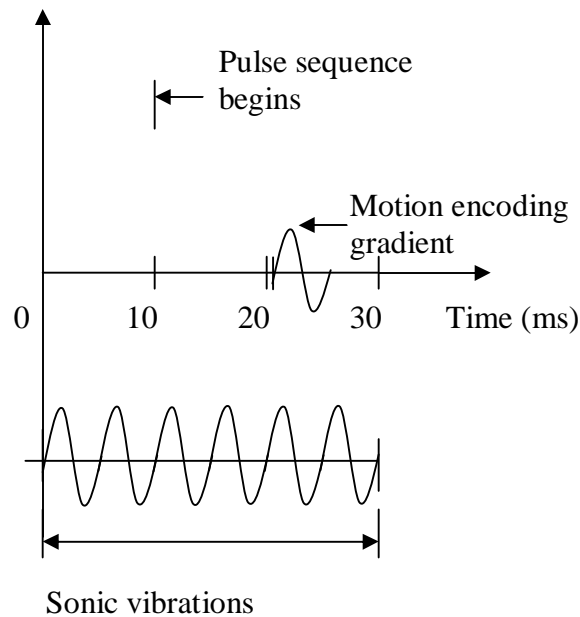


Fig 5.3 The 200Hz frequency vibrations start 10ms before the pulse sequence.

The phases of the two images with opposite gradient polarities were subtracted, yielding a phase encoded image for the applied vibration (Fig 5.4). Additionally, a stationary piece of gel was placed beside the phantom for purposes of normalization of any gross phase variations due to the system and the overall vibration of the phantom. Shear stiffness values were calculated using

$$\mu = \lambda^2 f^2 \rho, \quad [5.1]$$

where μ is the shear stiffness, λ is the wavelength of propagation, and ρ is the density of the gel, taken as 1.0 g/mL. The shear elasticity calculations assume negligible viscosity of the gel and isotropic tissue properties (119).

Measuring Stiffness as a Function of Temperature

A set of 1024 phase contrast images were obtained using SEA to capture harmonic transverse shear waves in an agarose gel phantom as heat was applied for 40 minutes with each frame spaced 2s apart. Following the elastography measurements, an experiment was performed using the proton resonance frequency (PRF) method to obtain temperature maps of the imaged slice also using SEA imaging. The PRF measurements

were performed using a gradient echo sequence with a TE/TR of 6ms/2500ms. Similar to the method for extracting encoded vibration data, encoded temperature data was obtained by subtracting each phase image from an initial phase image, which indicates the difference in temperature between the two frames. Room temperature was added to this data, giving the absolute temperature of the gel. Due to the destructive nature of the heating experiments, the PRF method was performed on a new phantom rather than the one imaged for elastography. The two phantoms were constructed identically, except the vibrating plate was omitted from the latter. Due to the greater sensitivity of the gradient echo sequence to B_0 field inhomogeneities, a relay was employed to stop current to the halogen lamp for 100 ms during each SEA image acquisition. A time of 100ms was used to provide sufficient time to overcome the mechanical latency of the relay. PRF measurements were not acquired simultaneous to elastography due to the added complexity of signal processing required to separate the PRF and elastography data, both of which are encoded into the phase images.

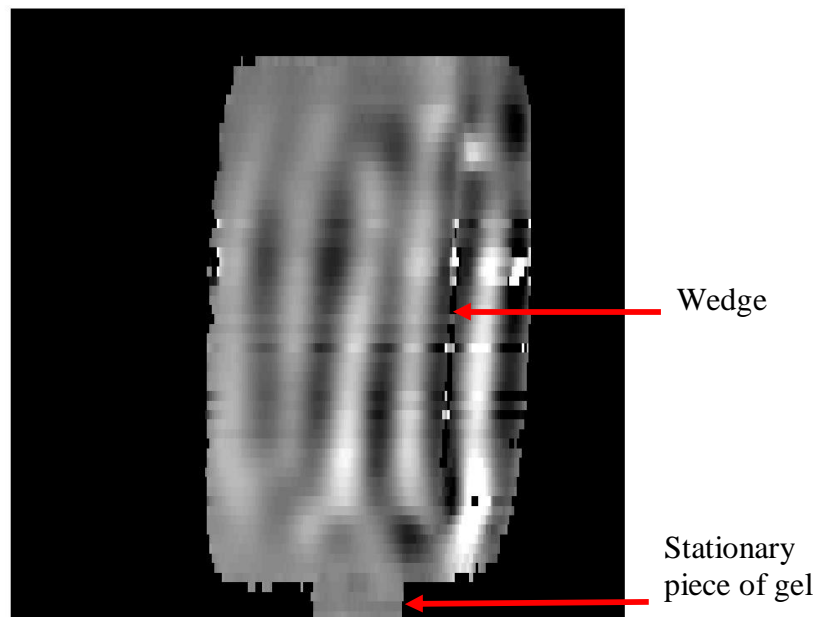


Fig 5.4 A phase contrast image obtained from subtracting two SEA images with positive and negative motion encoding gradients. Each 256 X 64 SEA image was obtained in a single shot.

V.2.2 Results

The MRE images of the phantom at time instances of 10, 20, 30 and 40 minutes are shown in Fig 5. The images show a change in the wavelength of the shear waves with change in temperature.

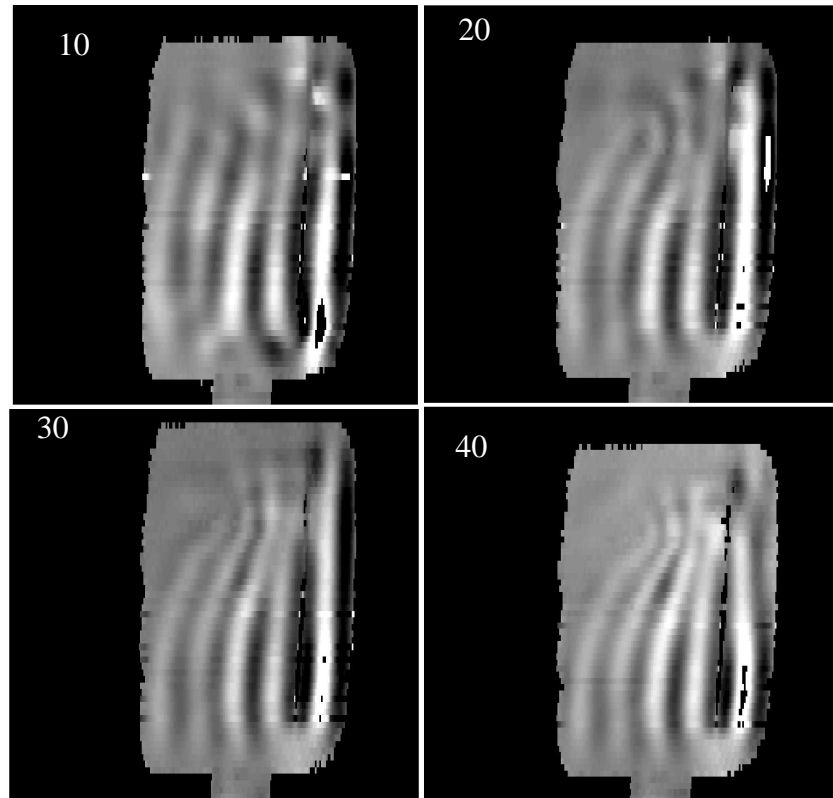


Fig 5.5 Shown are four phase contrast images at time instances of 10, 20, 30 and 40 minutes from the beginning of the heating. The images show a shrinking in the wavelength of the shear waves with increasing temperature.

The movie clearly depicts the changing wavelength of the shear waves as time progressed and the gel grew warmer. There was a spatial distribution of wavelengths corresponding to the spatial distribution of temperature as the gel was heated. Fig 5.6 shows the different steps in processing the data in obtaining the shear stiffness distribution as a function of the temperature. A region of interest of size 103x28 was chosen to calculate the wavelengths and shear modulus. The wavelengths of the shear waves were obtained by calculating the spacing between the troughs of the phase profile corresponding to each row in the region of interest (Fig 5.6(b)). Due to size constraints, only four periods of vibration were captured in each image. As the gel was heated, these waves only

propagated into an area of roughly one half of the phantom, so attempting to determine the wavelength at every point along each row of the image was not meaningful. Because it was observed that there is little variation of wavelength along a row, it was assumed to be constant. The variation was significant between the rows and in the temporal dimension. The temporal variation of the wavelength corresponding to a row is shown in Fig 5.6(c). A 10th order polynomial function was fit to smooth out the data. The average mean square error because of the fit was 0.87mm and the average standard deviation was 0.8mm. The time dependency of the wavelength corresponding to the 30 rows in the region of interest were computed and the shear modulus was calculated using the formula $\mu = \lambda^2 f^2 \rho$. A waterfall diagram of the temporal variations of the shear stress for all the 30 rows is shown in Fig 5.6(d). The spatial and temporal distribution of temperature was then obtained using the proton resonance frequency method (Fig 5.7).

V.2.3 Discussion

The waterfall plot in figure 6 shows a consistent drop in shear modulus for all channels with increasing temperature. This trend agrees well with results reported in literature for bovine tissue during thermal ablation (116). To validate the argument that the reason behind a drop in shear modulus is the temperature, the variation in two different rows is compared (Figure 5.8). The portion of the gel closer to the heat source (row 3) shows a much greater drop in shear modulus when compared to row 26 which is further way from the heat source. This trend is also seen in Fig 5.9., which shows the shear modulus for each row of the ROI of frame 1 and frame 950. Frame 1 was much cooler and stiffer than frame 950. Also, it can be seen that within the frame 950, the rows that are closer to the heat gel have lower shear stiffness when compared to regions away from the heat source. The reason for sudden jump in the shear modulus at around frame 205 is not clearly understood at this point in time and will be investigated in the future.

Our method acquires pairs of images using a spin echo sequence with positive and negative motion sensitizing gradient waveforms. Acquisition of these pairs of images are temporally spaced sufficiently to allow the gel to heat, which was constrained by the

amount of current passing through the halogen lamp, as greater current destroys the filament of the lamp and creates local B_0 inhomogeneities.

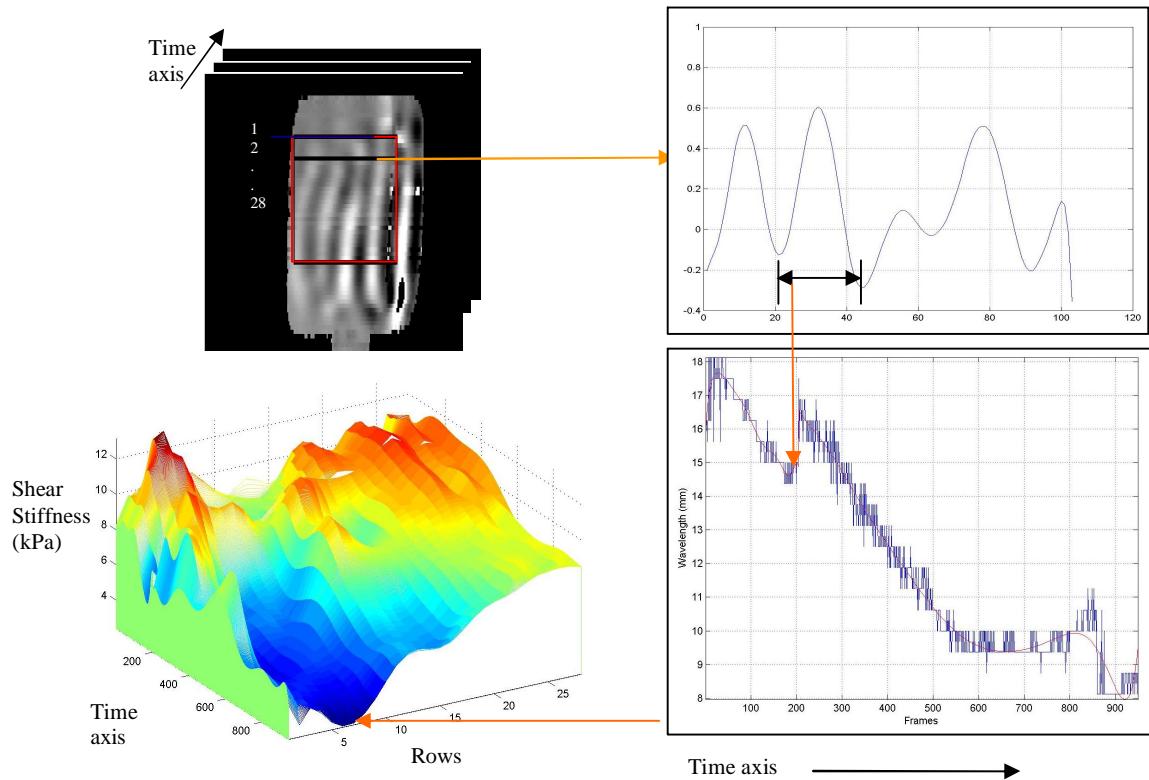


Fig 5.6 The Elastograms are obtained for a selected region of interest (ROI). The wavelengths of the shear waves are calculated for each row in the ROI and for every frame. The shear modulus is calculated using the formula

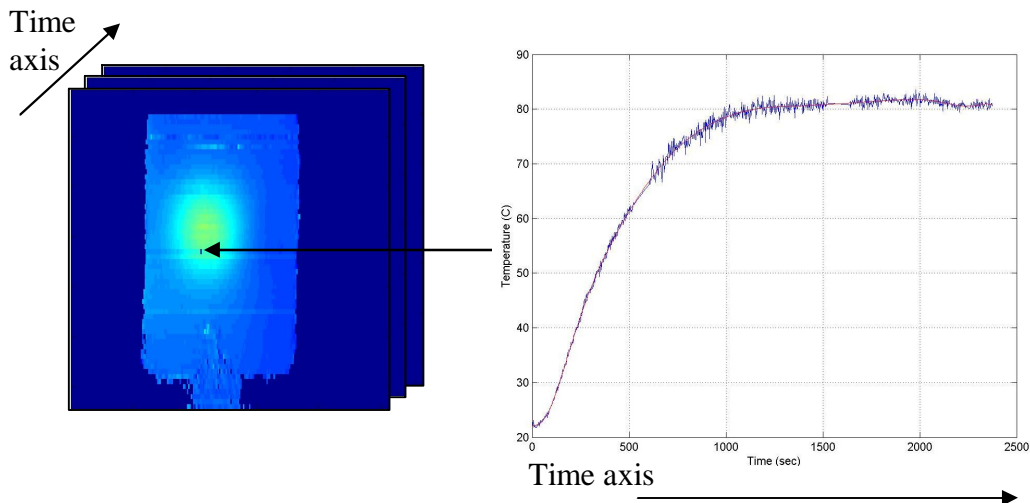


Fig 5.7 The temperature was obtained using the PRF method. Also shown is the temperature of a point in the gel as a function of time.

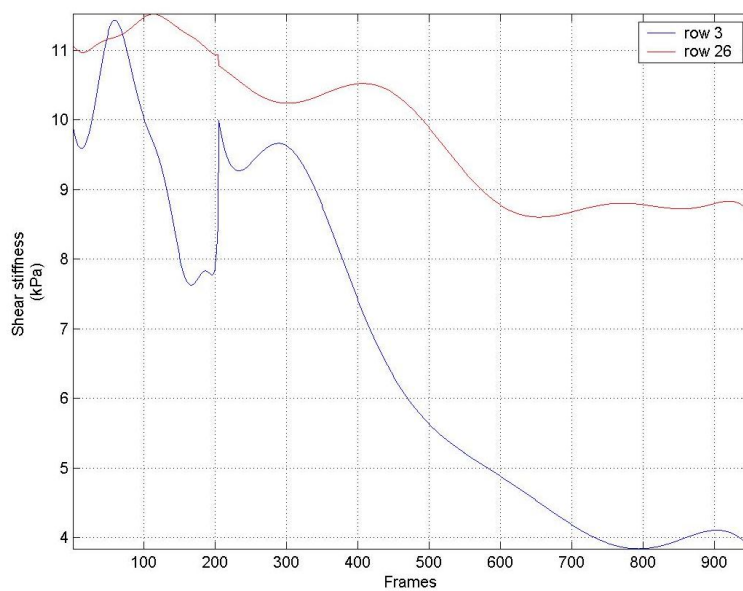


Fig 5.8 The drop in shear modulus with time is greater in portions of the gel closer to the heat source (row 3) when compared to the ones further away (row 26).

Many methods of calculating the shear modulus from the phase images have been proposed (120). In this study, however, we used a simple technique of extracting the wavelengths assuming the wavelength to remain constant in one (x-axis) direction of a

frame. The rationale being, quantifying any changes in wavelength with just three shear waves along the x-direction may not be accurate. But, the variation of wavelength and hence the shear modulus along the y-direction may provide insight into the variation along the x-direction because of the symmetric nature of the heat source (Fig 5.9). The number of shear waves had to be limited to three to avoid interference from waves reflected off the boundaries. One of the methods to accommodate more number of waves and get a spatial variation of the wavelength is to use acoustic vibrations of a higher frequency.

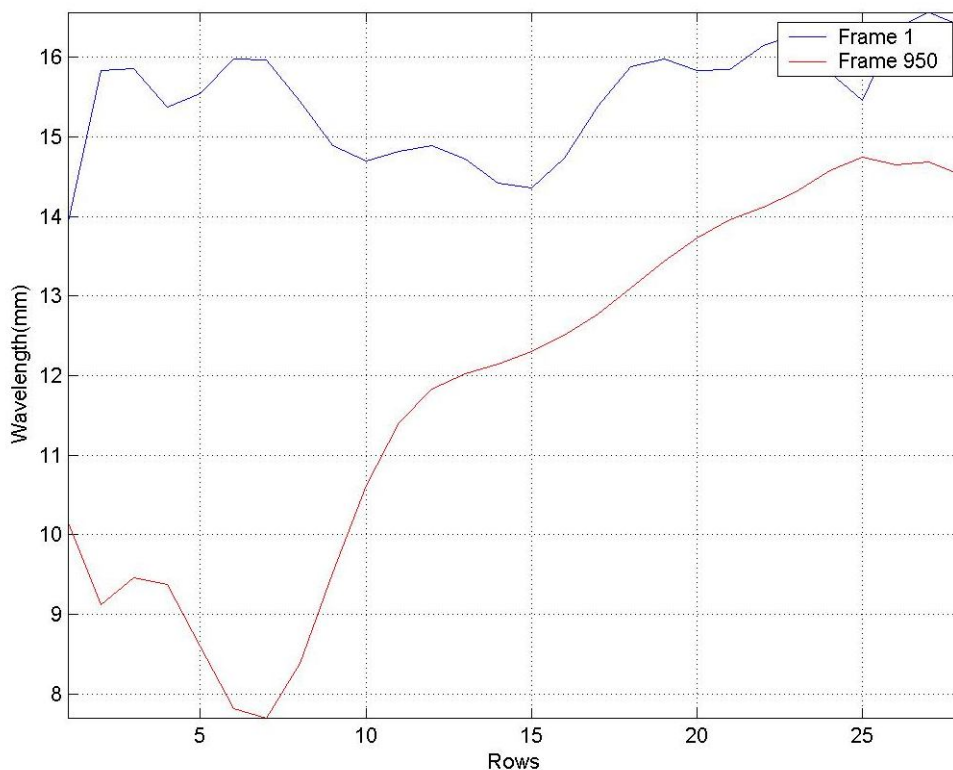


Fig 5.9 Comparison of shear modulus of the ROI in frame 1 and frame 950. Frame 950 being much warmer than frame 1, shows a reduced shear modulus when compared to frame 1. Also regions in frame 950 closer to the heat source have reduced shear modulus compared to the ones further away.

Taking advantage of the low frame rate as a result of a low power heat source, spin echo sequence was used in this demonstration to reduce the effects of field inhomogeneities. A gradient echo sequence could also be employed to reduce acquisition time and the PRF data can be interleaved along with the motion encoding gradients, as both are encoded in phase. Additionally, if the structure does not change significantly during heating,

elastography displacement maps can be generated by subtracting the phase of a series of images from a single reference image, eliminating the need to acquire pairs of images (74). In the past, our group has demonstrated the ability to image at ultra high frame rates of 200 frames per second with gradient echo techniques. Methods of rapidly heating the gel without disturbing the magnetic field, such as with a heat conducting fluid, lasers or FUS, will provide motivation for further increasing the image acquisition rate. However, the limiting factor in acquisition frame rate then becomes the length of time necessary for the motion sensitizing gradient waveform, which is typically at least one period of the acoustic vibration frequency. Taking into account the time needed for motion encoding and the time needed for the waves to attenuate between successive acquisitions, a repetition rate of 20 frames per second is feasible.

Future work will attempt to overcome this limitation by imaging without a frequency selective motion sensitizing gradient, relying instead on the velocity information encoded by the phase compensation gradient. This will require imaging at a rate fast enough to observe the changing displacements of the individual voxels as the acoustic wave propagates. It will provide a better “snapshot” of the motion, avoiding any averaging due to the length of time normally required to encode phase into the vibrating gel. Methods to validate the temperature measurements using PRF also have to be done. One of the solutions here is using fluoro-optic sensors.

We have demonstrated that SEA imaging can be used to construct elastography animations at a rate of a single frame per echo, enabling the rapid acquisition of transient events. This could be important in cases where material fatigue or other mechanisms make repetition difficult. The study also demonstrates the feasibility where the tissue characteristics for rapid heating and cooling can be quantified.

CHAPTER VI

FUTURE WORK AND CONCLUSIONS

There are two parts to this research project. The previous chapters discussed both of these, the building of a 64 channel SEA MRI reconstruction system and its applications. With the ability to digitally demodulate 200 frames per second, this is the fastest MRI system built so far. The model is easily scalable to accommodate any number of channels. The model is a combination of digitization and processing power. The large amounts of data generated during digitization were processed using time efficient and elegant algorithms, which enabled the concept of real-time imaging. Also, implemented in the project is a new technique that reduces the digitized data by a significant amount by minimizing the sampling rate. The reduced sampling rate can further improve the number of frames processed per second. An interesting question in this scenario is, what do we observe at such high frame rates? Intrinsic material properties such as T1, T2 are of the order of a few hundred milliseconds, so changes of the order of a millisecond do not correspond to changes in these time constants. The answer can however be in the temperature dependent MRE experiments done. Capturing dynamically changing material properties at high frame rates provide insight into their behavior which could be very non-linear.

For many research groups looking to employ large number of receiver channels, the reduced sampling technique could prove beneficial. The primary objective of using the DSP board in our case is because of the dedicated data bus it provides, apart from the dedicated processing power. With significantly small amount of data generated with the reduced sampling technique, a dedicated bus to move the data and hence a DSP board may not be needed. Improvements in PCI bus technology also helps in downloading the digitized data to the memory. As far as the computation power is concerned, the currently available CPU power with dual and quad core technologies can easily support multi channel digitizers. The current system can also be made equipped with a quad cluster to measure any improvements in processing time. The recent years have also seen major advancements in digitization technology. The latest state-of-the-art digitizers sample at 2GSamples/s and use the PXI bus, which is much faster than the PCI (83). The number of

cards are scalable and rackmountable to accommodate large number of channels. These technologies are suitable for digitizing the NMR signal without any down conversion. Few of the potential issues could be the amount of data that is generated, the processing of all that data and the memory limitations onboard.

Using the SEA technology and the tool that has been built, we have discovered the primary area where this technology can be put to a great use. Experiments involving short-life events, destructive events, non-recoverable events can be captured at high frame rates. One of the promising areas of applications discussed in this project is the SEA MRE technique. The thermal ablation experiment was chosen because of its self-destructive nature. Using acoustic vibrations, SEA MRI was able to quantify the temperature dependency of tissues shear stiffness. This experiment has been done as an exploratory study. The feasibility of being able to measure the shear modulus has been demonstrated. One of the future directions in this area is to quantify the shear stiffness by using a rapid heating setup that would ramp up the temperature of the gel. This can be achieved with the use of lasers, focused ultrasound, etc. More number of shear waves can also induced in the gel to a better assessment of the spatial resolution of the shear modulus. Also, acoustic vibrations of different frequencies can be tried for a characterization of the dependency of shear modulus with frequency. Another direction in SEA MRE could be the rapid cooling of gels. In all of these experiments an accurate metric of temperature is needed. One of the reliable and accurate measurements of temperature, fluoro-optic sensors, can be used to quantify the temperature.

REFERENCES

1. Ordidge RJ, Mansfield P, Doyle M, Coupland RE. Real time movie images by NMR. *British Journal of Radiology* 1982;55(658):729-733.
2. Stehling M, Howseman A, Chapman B, Coxon R, Glover P, Turner R, Ordidge RJ, Jaroszkiewicz G, Mansfield P, Morris GK, et al. Real-time NMR imaging of coronary vessels. *Lancet* 1987;2(8565):964-965.
3. Ordidge RJ, Howseman A, Coxon R, Turner R, Chapman B, Glover P, Stehling M, Mansfield P. Snapshot imaging at 0.5 T using echo-planar techniques. *Magn Reson Med* 1989;10(2):227-240.
4. Stehling MJ, Howseman AM, Ordidge RJ, Chapman B, Turner R, Coxon R, Glover P, Mansfield P, Coupland RE. Whole-body echo-planar MR imaging at 0.5 T. *Radiology* 1989;170(1 Pt 1):257-263.
5. Stehling MK, Evans DF, Lamont G, Ordidge RJ, Howseman AM, Chapman B, Coxon R, Mansfield P, Hardcastle JD, Coupland RE. Gastrointestinal tract: dynamic MR studies with echo-planar imaging. *Radiology* 1989;171(1):41-46.
6. Stehling MK, Charnley RM, Blamire AM, Ordidge RJ, Coxon R, Gibbs P, Hardcastle JD, Mansfield P. Ultrafast magnetic resonance scanning of the liver with echo-planar imaging. *Br J Radiol* 1990;63(750):430-437.
7. Stehling MK, Turner R, Mansfield P. Echo-planar imaging: magnetic resonance imaging in a fraction of a second. *Science* 1991;254(5028):43-50.
8. Edelman RR, Wielopolski P, Schmitt F. Echo-planar MR imaging. *Radiology* 1994;192(3):600-612.
9. Frahm J. Rapid FLASH NMR imaging. *Die Naturwissenschaften* 1987;74(9):415-422.
10. Frahm J, Haase A, Matthaei D. Rapid NMR imaging of dynamic processes using the FLASH technique. *Magn Reson Med* 1986;3(2):321-327.
11. Frahm J, Haase A, Matthaei D. Rapid three-dimensional MR imaging using the FLASH technique. *Journal of Computer Assisted Tomography* 1986;10(2):363-368.
12. Farzaneh F, Riederer SJ, Lee JN, Tasciyan T, Wright RC, Spritzer CE. MR fluoroscopy: initial clinical studies. *Radiology* 1989;171(2):545-549.
13. Riederer SJ, Tasciyan T, Farzaneh F, Lee JN, Wright RC, Herfkens RJ. MR fluoroscopy: technical feasibility. *Magn Reson Med* 1988;8(1):1-15.
14. Holsinger AE, Wright RC, Riederer SJ, Farzaneh F, Grimm RC, Maier JK. Real-time interactive magnetic resonance imaging. *Magn Reson Med* 1990;14(3):547-553.
15. Spritzer CE, Pelc NJ, Lee JN, Evans AJ, Sostman HD, Riederer SJ. Rapid MR imaging of blood flow with a phase-sensitive, limited-flip-angle, gradient recalled pulse sequence: preliminary experience. *Radiology* 1990;176(1):255-262.
16. Wright RC, Riederer SJ, Farzaneh F, Rossman PJ, Liu Y. Real-time MR fluoroscopic data acquisition and image reconstruction. *Magn Reson Med* 1989;12(3):407-415.

17. Roschmann P. Radiofrequency penetration and absorption in the human body: limitations to high-field whole-body nuclear magnetic resonance imaging. *Med Phys* 1987;14(6):922-931.
18. Hutchinson M, Raff U. Fast MRI data acquisition using multiple detectors. *Magn Reson Med* 1988;6(1):87-91.
19. Carlson JW, Minemura T. Imaging time reduction through multiple receiver coil data acquisition and image reconstruction. *Magn Reson Med* 1993;29(5):681-687.
20. Kwiat D, Einav S, Navon G. A decoupled coil detector array for fast image acquisition in magnetic resonance imaging. *Med Phys* 1991;18(2):251-265.
21. Kwiat D, Einav S. Preliminary experimental evaluation of an inverse source imaging procedure using a decoupled coil detector array in magnetic resonance imaging. *Medical Engineering & Physics* 1995;17(4):257-263.
22. Sodickson DK, Manning WJ. Simultaneous acquisition of spatial harmonics (SMASH): fast imaging with radiofrequency coil arrays. *Magn Reson Med* 1997;38(4):591-603.
23. Wright SM, Wald LL. Theory and application of array coils in MR spectroscopy. *NMR Biomed* 1997;10(8):394-410.
24. Pruessmann KP, Weiger M, Scheidegger MB, Boesiger P. SENSE: sensitivity encoding for fast MRI. *Magn Reson Med* 1999;42(5):952-962.
25. Bankson JA, Griswold MA, Wright SM, Sodickson DK. SMASH imaging with an eight element multiplexed RF coil array. *Magma* 2000;10(2):93-104.
26. Griswold MA, Jakob PM, Heidemann RM, Nittka M, Jellus V, Wang J, Kiefer B, Haase A. Generalized autocalibrating partially parallel acquisitions (GRAPPA). *Magn Reson Med* 2002;47(6):1202-1210.
27. Griswold MA, Jakob PM, Nittka M, Goldfarb JW, Haase A. Partially parallel imaging with localized sensitivities (PILS). *Magn Reson Med* 2000;44(4):602-609.
28. Zhu Y, Hardy CJ, Sodickson DK, Giaquinto RO, Dumoulin CL, Kenwood G, Niendorf T, Lejay H, McKenzie CA, Ohliger MA, Rofsky NM. Highly parallel volumetric imaging with a 32-element RF coil array. *Magn Reson Med* 2004;52(4):869-877.
29. McDougall MP, Wright SM. 64-channel array coil for single echo acquisition magnetic resonance imaging. *RF,Real-Time Magn Reson Med* 2005;54(2):386-392.
30. Sodickson DK, Hardy CJ, Zhu Y, Giaquinto RO, Gross P, Kenwood G, Niendorf T, Lejay H, McKenzie CA, Ohliger MA, Grant AK, Rofsky NM. Rapid volumetric MRI using parallel imaging with order-of-magnitude accelerations and a 32-element RF coil array: feasibility and implications. *Academic Radiology* 2005;12(5):626-635.
31. Jakob PM, Griswold MA, Edelman RR, Sodickson DK. AUTO-SMASH: a self-calibrating technique for SMASH imaging. *SiMultaneous acquisition of spatial harmonics. Magma* 1998;7(1):42-54.

32. Heidemann RM, Griswold MA, Haase A, Jakob PM. VD-AUTO-SMASH imaging. *Magn Reson Med* 2001;45(6):1066-1074.
33. Barkhausen J, Quick HH, Lauenstein T, Goyen M, Ruehm SG, Laub G, Debatin JF, Ladd ME. Whole-body MR imaging in 30 seconds with real-time true FISP and a continuously rolling table platform: feasibility study. *Radiology* 2001;220(1):252-256.
34. Bodurka J, Ledden PJ, van Gelderen P, Chu R, de Zwart JA, Morris D, Duyn JH. Scalable multichannel MRI data acquisition system. *Magn Reson Med* 2004;51(1):165-171.
35. D'Amico AV, Cormack R, Tempny CM, Kumar S, Topulos G, Kooy HM, Coleman CN. Real-time magnetic resonance image-guided interstitial brachytherapy in the treatment of select patients with clinically localized prostate cancer. *Int J Radiat Oncol Biol Phys* 1998;42(3):507-515.
36. Hanlon AD, Gibbs SJ, Hall LD, Haycock DE, Frith WJ, Ablett S. Rapid MRI and velocimetry of cylindrical Couette flow. *Magn Reson Imaging* 1998;16(8):953-961.
37. Hardy CJ, Darrow RD, Pauly JM, Kerr AB, Dumoulin CL, Hu BS, Martin KM. Interactive coronary MRI. *Magn Reson Med* 1998;40(1):105-111.
38. Hardy CJ, Darrow RD, Saranathan M, Giaquinto RO, Zhu Y, Dumoulin CL, Bottomley PA. Large field-of-view real-time MRI with a 32-channel system. *Magn Reson Med* 2004;52(4):878-884.
39. Naganawa S, Ishiguchi T, Ishigaki T, Sato K, Katagiri T, Kishimoto H, Mimura T, Takizawa O, Imura C. Real-time interactive MR imaging system: sequence optimization, and basic and clinical evaluations. *Radiat Med* 2000;18(1):71-79.
40. Omary RA, Unal O, Koscielski DS, Frayne R, Korosec FR, Mistretta CA, Strother CM, Grist TM. Real-time MR imaging-guided passive catheter tracking with use of gadolinium-filled catheters. *J Vasc Interv Radiol* 2000;11(8):1079-1085.
41. Rasche V, de Boer RW, Holz D, Proksa R. Continuous radial data acquisition for dynamic MRI. *Magn Reson Med* 1995;34(5):754-761.
42. Rasche V, Holz D, Kohler J, Proksa R, Roschmann P. Catheter tracking using continuous radial MRI. *Magn Reson Med* 1997;37(6):963-968.
43. Riederer SJ, Fain SB, Kruger DG, Busse RF. Real-time imaging and triggering of 3D contrast-enhanced MR angiograms using MR fluoroscopy. *Magma* 1999;8(3):196-206.
44. Saam B, Yablonskiy DA, Gierada DS, Conradi MS. Rapid imaging of hyperpolarized gas using EPI. *Magn Reson Med* 1999;42(3):507-514.
45. Wright SM, McDougall MP, Yallapragada N. Rapid Flow Imaging Using Single Echo Acquisition MRI. Proc 13th Annual Meeting ISMRM, Miami, 2005. p289.
46. Morgan PN, Iannuzzelli RJ, Epstein FH, Balaban RS. Real-time cardiac MRI using DSP's. *IEEE Trans Med Imaging* 1999;18(7):649-653.

47. Bock M, Muller S, Zuehlsdorff S, Speier P, Fink C, Hallscheidt P, Umathum R, Semmler W. Active catheter tracking using parallel MRI and real-time image reconstruction. *Magn Reson Med* 2006;55(6):1454-1459.
48. Weiger M, Pruessmann KP, Boesiger P. Cardiac real-time imaging using SENSE. SENSitivity Encoding scheme. *Magn Reson Med* 2000;43(2):177-184.
49. Hoenninger JC, Crooks LE, Arakawa M. A floating-point digital receiver for MRI. *IEEE Trans Biomed Eng* 2002;49(7):689-693.
50. Holland GN, MacFall JR. An overview of digital spectrometers for MR imaging. Instrumentation Subcommittee of the SMRI Basic Science Council. *J Magn Reson Imaging* 1992;2(2):241-246.
51. Wiggins GC, Potthast A, Triantafyllou C, Lin F, Benner T, Wiggins CJ, Wald LL. A 96-channel MRI System with 23- and 90-channel Phase Array Head Coils at 1.5 Tesla. Proc 13th Annual Meeting ISMRM, Miami, 2005. p 671.
52. Wiggins GC, Triantafyllou C, Potthast A, Reykowski A, Nittka M, Wald LL. 32-channel 3 Tesla receive-only phased-array head coil with soccer-ball element geometry. *Magn Reson Med* 2006;56(1):17.
53. Lindon JC, Ferrige AG. Digitisation and data processing in Fourier transform NMR. *Progress in Nuclear Magnetic Resonance Spectroscopy* 1980;14:27-66.
54. Hoult DI. The NMR receiver: A description and analysis of design. *Progress in Nuclear Magnetic Resonance Spectroscopy* 1978;12(1):41-77.
55. Wittebort RJ, Woehler SE, Bradley CH. Efficient probe and receiver for solid-state ²H NMR. *Journal of Magnetic Resonance* 1986;67(1):143-147.
56. Villa M, Tian F, Cofrancesco P, Halamek J, Kasal M. High-resolution digital quadrature detection. *Review of Scientific Instruments* 1996;67(6):2123-2129.
57. Kasal M, Halamek J, Husek V, Villa M, Ruffina U, Cofrancesco P. Signal processing in transceivers for nuclear magnetic resonance and imaging. *Review of Scientific Instruments* 1994;65(6):1897-1902.
58. Gengying L, Haibin X. Digital quadrature detection in nuclear magnetic resonance spectroscopy. *Review of Scientific Instruments* 1999;70(2):1511-1513.
59. Qin X, Jie S, Jianqi L, Gengying L. Compensation for unknown acquisition delay caused by digital receiver without external synchronization in NMR and MRI. *Magma* 2005;18(4):217-224.
60. Michal CA, Broughton K, Hansen E. A high performance digital receiver for home-built nuclear magnetic resonance spectrometers. *Review of Scientific Instruments* 2002;73(2):453-458.
61. Brown DG, McDougall MP, Wright SM. Receiver design for parallel imaging with large arrays. Proc 10th Annual Meeting ISMRM, Honolulu, 2002.p 863.
62. Lauterbur PC. Image Formation by Induced Local Interactions: Examples Employing Nuclear Magnetic Resonance. *Nature* 1973;242(5394):190-191.

63. Rane SD. Parallel magnetic resonance imaging: Characterization and comparison, M.S. Thesis, Texas A&M University, College Station, 2005. 68 p.
64. McDougall MP. Single echo acquisition magnetic resonance imaging, Ph.D. Dissertation, Texas A&M University, College Station, 2004. 122 p.
65. Brown DG. Instrumentation for parallel magnetic resonance imaging, Ph.D. Dissertation, Texas A&M University, College Station, 2005. 277 p.
66. ICS-645. 32-Channel, 2.5 MHz/ch., 16-Bit Oversampling ADC Board. Available at <http://www.ics-ltd.com/info/productInfo.cfm?prodID=19&pCatID=1>.
67. AD9260. Analog Devices, 16-Bit High Speed Oversampled A/D Converter Rev C. Available at <http://www.analog.com/en/prod/0,,AD9260,00.html>. Magma (New York, NY).
68. McDougall MP, Wright SM. Phase compensation in single echo acquisition imaging. Phase effects of voxel-sized coils in planar and cylindrical arrays. *IEEE Eng Med Biol Mag* 2005;24(6):17-22.
69. TS-P36N. Quad ADSP-TS101 PCI with FPGA I/O. Available at <http://www.vsystems.com/category3075.html>.
70. Remezord. Available at http://www.mathworks.com/access/helpdesk_r13/help/toolbox/signal/remezord.html.
71. Yallapragada N, Wright SM, McDougall MP. A Compact 64 Channel Real-Time MRI Reconstruction System. *Proc 13th Annual Meeting ISMRM*, Miami, 2005. p862.
72. Wright SM, McDougall MP, Yallapragada N. Ultra-Fast MR Velocity Measurement using Spin-Tagging and Single-Echo Acquisition (SEA) Imaging. *Proc 14th Annual Meeting ISMRM*, Seattle, 2006. p 203.
73. McDougall MP, Wright SM, Steele-Russell I, Yallapragada N, Russell M. Rapid Large Field-of-View Microscopy Using Parallel Imaging. *Proc 14th Annual Meeting ISMRM*, Seattle, 2006. p 2448.
74. Bosshard JC, Yallapragada N, McDougall MP, Wright SM. High Speed MR Elastography Using SEA Imaging. *Proc 16th Annual Meeting ISMRM*, Toronto, 2008. 2008.
75. McDougall MP, Wright SM. 64-channel array coil for single echo acquisition magnetic resonance imaging. *Magn Reson Med* 2005;54(2):386-392.
76. GC4016. Multi-Standard QUAD DDC Chip Data Sheet. Revision 1.0. Available at <http://www.ti.com/graychip/GC4016/GC4016.html>.
77. Wright SM, Brown DG, Porter JR, Spence DC, Esparza E, Cole DC, Huson FR. A desktop magnetic resonance imaging system. *Magma* 2002;13(3):177-185.
78. Morris H, Derbyshire JA, Kellman P, Chesnick AS, Guttman MA, ER M. A wide-bandwidth multi-channel digital receiver and real-time reconstruction engine for use with a clinical MR scanner. *Proc 10th Annual Meeting ISMRM*, Honolulu, 2002. p 61.

79. Wei J, Liu Z, Chai Z, Yuan J, Lian J, Shen GX. A realization of digital wireless transmission for MRI signals based on 802.11b. *J Magn Reson* 2007;186(2):358-363.
80. Yallapragada N, Wright SM. Reducing data handling issues in large coil arrays by '1F' undersampling. *Proc 15th Annual Meeting ISMRM, Berlin, 2007.* p 989.
81. Krohn-Hite Corp, Model 3940 3Hz to 2MHz, 24dB/Octave 2-ch LP/HP Butterworth/Bessel Progr. Filter, Brockton, MA. Available: <http://www.krohn-hite.com/>.
82. Analog Devices, Inc., AD6645 14-Bit 80 MSPS/105 MSPS A/D Converter, Norwood, MA. Available: <http://www.analog.com/en/prod/0,2877,AD6645,00.html>.
83. National Instruments Corp., NI PXI 5152 Specification 8-bit, 2 GS/s digitizer, Austin, TX.
84. Muthupillai R, Lomas DJ, Rossman PJ, Greenleaf JF, Manduca A, Ehman RL. Magnetic resonance elastography by direct visualization of propagating acoustic strain waves. *Science* 1995;269(5232):1854-1857.
85. Muthupillai R, Rossman PJ, Lomas DJ, Greenleaf JF, Riederer SJ, Ehman RL. Magnetic resonance imaging of transverse acoustic strain waves. *Magn Reson Med* 1996;36(2):266-274.
86. Greenleaf JF, Muthupillai R, Rossman PJ, Smith J, Manduca A, Ehman RL. Direct visualization of strain waves by Magnetic Resonance Elastography (MRE). *Proc. of the IEEE Ultrasonics Symposium, San Antonio, 1996.* p 467-72.
87. Lewa CJ, De Certaines JD. Viscoelastic property detection by elastic displacement NMR measurements. *J Magn Reson Imaging* 1996;6(4):652-656.
88. Dutt V, Kinnick RR, Muthupillai R, Oliphant TE, Ehman RL, Greenleaf JF. Acoustic shear-wave imaging using echo ultrasound compared to magnetic resonance elastography. *Ultrasound Med Biol* 2000;26(3):397-403.
89. Sandrin L, Catheline S, Tanter M, Hennequin X, Fink M. Time-resolved pulsed elastography with ultrafast ultrasonic imaging. *Ultrasonic Imaging* 1999;21(4):259-272.
90. Kruse SA, Smith JA, Lawrence AJ, Dresner MA, Manduca A, Greenleaf JF, Ehman RL. Tissue characterization using magnetic resonance elastography: preliminary results. *Phys Med Biol* 2000;45(6):1579-1590.
91. Plewes DB, Bishop J, Samani A, Sciarretta J. Visualization and quantification of breast cancer biomechanical properties with magnetic resonance elastography. *Phys Med Biol* 2000;45(6):1591-1610.
92. Kemper J, Sinkus R, Lorenzen J, Nolte-Ernsting C, Stork A, Adam G. MR elastography of the prostate: initial in-vivo application. *Rofo* 2004;176(8):1094-1099.
93. Huwart L, Peeters F, Sinkus R, Annet L, Salameh N, ter Beek LC, Horsmans Y, Van Beers BE. Liver fibrosis: non-invasive assessment with MR elastography. *NMR Biomed* 2006;19(2):173-179.
94. Sack I, Bernarding J, Braun J. Analysis of wave patterns in MR elastography of skeletal muscle using coupled harmonic oscillator simulations. *Magn Reson Imaging* 2002;20(1):95-104.

95. Bensamoun SF, Ringleb SI, Littrell L, Chen Q, Brennan M, Ehman RL, An KN. Determination of thigh muscle stiffness using magnetic resonance elastography. *J Magn Reson Imaging* 2006;23(2):242-247.
96. Hamhaber U, Grieshaber FA, Nagel JH, Klose U. Comparison of quantitative shear wave MR-elastography with mechanical compression tests. *Magn Reson Med* 2003;49(1):71-77.
97. Sinkus R, Tanter M, Catheline S, Lorenzen J, Kuhl C, Sondermann E, Fink M. Imaging anisotropic and viscous properties of breast tissue by magnetic resonance-elastography. *Magn Reson Med* 2005;53(2):372-387.
98. Sinkus R, Tanter M, Xydeas T, Catheline S, Bercoff J, Fink M. Viscoelastic shear properties of in vivo breast lesions measured by MR elastography. *Magn Reson Imaging* 2005;23(2):159-165.
99. Uffmann K, Maderwald S, Ajaj W, Galban CG, Mateiescu S, Quick HH, Ladd ME. In vivo elasticity measurements of extremity skeletal muscle with MR elastography. *NMR Biomed* 2004;17(4):181-190.
100. Jenkyn TR, Ehman RL, An KN. Noninvasive muscle tension measurement using the novel technique of magnetic resonance elastography (MRE). *Journal of Biomechanics* 2003;36(12):1917-1921.
101. Dresner MA, Rose GH, Rossman PJ, Muthupillai R, Manduca A, Ehman RL. Magnetic resonance elastography of skeletal muscle. *J Magn Reson Imaging* 2001;13(2):269-276.
102. Shah NS, Kruse SA, Lager DJ, Farrell-Baril G, Lieske JC, King BF, Ehman RL. Evaluation of renal parenchymal disease in a rat model with magnetic resonance elastography. *Magn Reson Med* 2004;52(1):56-64.
103. Rouviere O, Yin M, Dresner MA, Rossman PJ, Burgart LJ, Fidler JL, Ehman RL. MR elastography of the liver: preliminary results. *Radiology* 2006;240(2):440-448.
104. McCracken PJ, Manduca A, Felmlee J, Ehman RL. Mechanical transient-based magnetic resonance elastography. *Magn Reson Med* 2005;53(3):628-639.
105. Glaser KJ, Felmlee JP, Ehman RL. Rapid MR elastography using selective excitations. *Magn Reson Med* 2006;55(6):1381-1389.
106. Lewa CJ, Roth M, Nicol L, Franconi JM, de Certaines JD. A new fast and unsynchronized method for MRI of viscoelastic properties of soft tissues. *J Magn Reson Imaging* 2000;12(5):784-789.
107. Yuan L, Glaser KJ, Rouviere O, Gorny KR, Chen S, Manduca A, Ehman RL, Felmlee JP. Preliminary assessment of one-dimensional MR elastography for use in monitoring focused ultrasound therapy. *Phys Med Biol* 2007;52(19):5909-5919.
108. Maderwald S, Uffmann K, Galban CJ, de Greiff A, Ladd ME. Accelerating MR elastography: a multiecho phase-contrast gradient-echo sequence. *J Magn Reson Imaging* 2006;23(5):774-780.

109. Cline HE, Hynynen K, Watkins RD, Adams WJ, Schenck JF, Ettinger RH, Freund WR, Vetro JP, Jolesz FA. Focused US system for MR imaging-guided tumor ablation. *Radiology* 1995;194(3):731-737.
110. Hynynen K, Damianou C, Darkazanli A, Unger E, Schenck JF. The feasibility of using MRI to monitor and guide noninvasive ultrasound surgery. *Ultrasound Med Biol* 1993;19(1):91-92.
111. Hynynen K, Damianou CA, Colucci V, Unger E, Cline HH, Jolesz FA. MR monitoring of focused ultrasonic surgery of renal cortex: experimental and simulation studies. *J Magn Reson Imaging* 1995;5(3):259-266.
112. Cline HE, Schenck JF, Watkins RD, Hynynen K, Jolesz FA. Magnetic resonance-guided thermal surgery. *Magn Reson Med* 1993;30(1):98-106.
113. Graham SJ, Bronskill MJ, Henkelman RM. Time and temperature dependence of MR parameters during thermal coagulation of ex vivo rabbit muscle. *Magn Reson Med* 1998;39(2):198-203.
114. Sapareto SA, Dewey WC. Thermal dose determination in cancer therapy. *Int J Radiat Oncol Biol Phys* 1984;10(6):787-800.
115. Wu T, Felmlee JP, Greenleaf JF, Riederer SJ, Ehman RL. MR imaging of shear waves generated by focused ultrasound. *Magn Reson Med* 2000;43(1):111-115.
116. Wu T, Felmlee JP, Greenleaf JF, Riederer SJ, Ehman RL. Assessment of thermal tissue ablation with MR elastography. *Magn Reson Med* 2001;45(1):80-87.
117. Wu T, Felmlee JP. A quality control program for MR-guided focused ultrasound ablation therapy. *Journal of Applied Clinical Medical Physics / American College of Medical Physics* 2002;3(2):162-167.
118. Wu T, Kendell KR, Felmlee JP, Lewis BD, Ehman RL. Reliability of water proton chemical shift temperature calibration for focused ultrasound ablation therapy. *Med Phys* 2000;27(1):221-224.
119. Fatemi M, Manduca A, Greenleaf JF. Imaging elastic properties of biological tissues by low-frequency harmonic vibration. *Proceedings of the IEEE* 2003;91(10):1503-1519.
120. Manduca A, Muthupillai R, Rossman PJ, Greenleaf JF, Ehman RL. Image processing for magnetic resonance elastography. *Proceedings of SPIE - The International Society for Optical Engineering, Newport Beach, 1996.* p 616-623.

VITA

Naresh Yallapragada was born in Gadwal, India in 1979 to Sudhaker and Madhuri Yallapragada. He graduated with a Bachelor of Technology (Honors) degree from the Indian Institute of Technology, Kharagpur, in 2001 and with a Master of Science degree from the University of Illinois at Chicago in 2003. Currently, he is completing his doctoral research work, graduating in May 2008. Following his completion, he expects to join the MR industry.

For further information, Naresh can be contacted at his permanent address:

16-11-741/D/85,

Dilsukh Nagar,

Hyderabad, AP – 500036

India

Email: naresh360@gmail.com